METHODS FOR MODELLING CHANGES IN VISCOELASTICITY OF THE URINARY BLADDER BY ANATOMICAL LOCATION AND SWELLING

By

Laura Alison Nye

A THESIS

Submitted to
Michigan State University
in partial fulfillment of the requirements
for the degree of

Mechanical Engineering – Master of Science

2020

ABSTRACT

METHODS FOR MODELLING CHANGES IN VISCOELASTICITY OF THE URINARY BLADDER BY ANATOMICAL LOCATION AND SWELLING

By

Laura Alison Nye

Urinary bladder dysfunction affects millions worldwide. It adds burden to the healthcare system and individual patients with surgeries and long-term treatments such as daily catheterization. Patient specific modelling has been shown to reduce healthcare costs. Computational models are based on mechanical properties of tissues and can help in diagnoses or treatment plans. Although much work has been done on organs such as brain and heart, work on the urinary bladder is scarce. The bladder is a complex organ that exhibits time dependent behavior and so many factors must be considered when studying its mechanical properties.

Researchers face challenges in replicating others' experiments, isolating constituent behavior, identifying pathological causes of mechanical behavior, and modelling the viscoelasticity. We focus on two issues that will improve computational models of the urinary bladder wall. The first issue is to identify differences in mechanical behavior based on anatomical location and bath osmolarity. The second issue is to find an appropriate viscoelastic constitutive equation. Parameter characterization of viscoelastic models is especially challenging due to the time dependence of certain parameters. We explore the methods applied in literature and propose four possible models that would be appropriate for our experiment.

The models reveal that for best results, we must normalize our data, choose an appropriate relaxation spectrum that has a unique solution, and consider nonlinear elasticity in addition to viscoelasticity. Preliminary results from these models suggest that the lower body and trigone regions of the bladder have lower compliance than other regions. Our models also indicate a change in compliance based on bath osmolarity. In the future we will improve these results for definitive parameters that can be compared statistically. We will do this through the implementation of nonlinear elastic viscoelasticity and triphasic theory.

ACKNOWLEDGEMENTS

First and foremost, I would like to thank my advisor Dr. Sara Roccabianca, who has known me since I was an undergraduate and welcomed me to pursue a Master's degree while doing research in her lab. I have learned much from her over the past few years and am very thankful for all the time she has spent giving me guidance, reviewing my work, and being supportive overall.

I would also like to thank others who made this project possible: my thesis committee Dr. Tamara Reid Bush and Dr. Lik-Chuan Lee for their support, the creators of FEBio Gerard Ateshian and Steve Maas who answered many of my tedious questions, and Stacy Hollon in the Mechanical Engineering Department for helping me navigate many issues with patience and kindness.

My lab members Marissa Grobbel, Yuheng Wang, Dr. Sheng Chen, Tyler Tuttle, Dr. Mayank Sinha, and Eli Broemer supported me throughout this degree as well with brainstorming sessions and much needed breaks in the computer lab.

Lastly, I would like to thank my parents Linda Nye and Paul Nye, who instilled the importance of education in me since a young age and without whom this would not have been possible.

TABLE OF CONTENTS

LIST OF TABLES

LIST OF FIGURES

1. RATIONALE AND MATHEMATICAL BACKGROUND

1.1 Motivation: Urinary Bladder Dysfunction

Millions of people suffer from urinary bladder dysfunction and this condition has the potential to significantly decrease their quality of life and increase healthcare costs for them as individuals as well as for the US as a nation. Overactive bladder (OAB), underactive bladder (UAB), and neurogenic bladder are a few of the conditions requiring patients to accrue daily costs due to, for example, catherization or incontinence pads, and ultimately potentially major surgery. For example, one of the long-term solutions that are used to treat urinary incontinence is augmentation surgery. This procedure can potentially significantly increase bladder functionality and, ultimately, the quality of life of patients affected by incontinence. However, there is a somewhat high risk associated with it, in fact approximately 5% of patients undergoing this kind of surgery have repaired bladders rupture due to material incompatibility [Korossis et al., 2009]. Furthermore, Flack et al. (2015) pointed out that while surgical intervention may reduce costs long-term for an entire healthcare system, it is not usually financially feasible for individual patients. It was estimated in 2007 that the total cost of urinary incontinence in the United States was $65.9 billion for adults 25 years and older.

There is potential, however, for reducing this cost with patient specific modelling. This is shown, for example, by a study that used portable bladder ultrasounds to reduce catheter costs by 46% based on a "threshold volume" for each patient [Polliack et al., 2005]. This suggests that personalized medicine has great potential to decrease healthcare costs and increase the quality of care for each patient. To this end, in the last twenty years, other fields like cardiology and neurology have used mathematical modeling to generate patient-specific models that could significantly help clinicians with diagnosis and treatment choices. A widely used modeling technique, that has showed some level of success in other organs in the body such as the heart, brain, and skin, is finite element modelling (FEM) based on realistic mechanical description of tissues [Roccabianca and Bush, 2016]. The potential of these models is that they consider

how mechanical behavior of tissues changes due to age, sex, disease, injury, microstructure, and organ geometry, all of which have been identified as important factors in whole organ function.

Despite the enormous amount of literature on biomechanical modelling of soft biological tissues, work focusing on the urinary bladder (UB) has been largely overlooked. More accurate models are needed to predict the feasibility of tissue engineered scaffolds, preoperative planning for surgery, and preventive care. Theoretical modelling of urinary bladder tissue based on experimental data has a great potential to help diagnose disease, improve tissue engineered materials [Dahms et al., 1998], analyze interactions with medical devices [Natali et al., 2015], and ultimately contribute to the reduction of healthcare costs associated with urinary dysfunction.

1.2 Constitutive Model: Hyperelastic and Viscoelastic

It is well established that UB tissue has viscoelastic and hyperelastic behavior. Both viscoelasticity and hyperelasticity have been modelled in many papers on the UB [Fry and Wagg, 1999] [Nagatomi et al., 2004] [Nagatomi et al., 2008] [Van Mastrigt and Nagtegaal, 1981] [Thiruchelvam et al., 2003] [Natali et al, 2015]. Hyperelastic models are suitable to describe experimental data collected under pseudo-static conditions and are incapable of describing stress-relaxation experiments on their own. Similarly, linear viscoelastic models are only suitable to describe strains less than 0.1 [Vincent, 2012] and do not model stress-relaxation of the UB sufficiently. This can be observed in stress-relaxation experiments involving multiple strain increases.

In a stress-relaxation test of UB tissue, after the initial strain, a sharp decline in stress is observed, followed by a time dependent stress reduction until the sample becomes fully relaxed (**Figure 1**). At equilibrium, the elastic component of the tissue is the only contributor to stress, according to quasilinear viscoelasticity (QLV) theory [Fung, 1981]. If the elastic component behaved in a purely linear way, a second strain would produce a stress at equilibrium that is linearly proportional to the strain increase. However, this is not the

case in our experimental data (**Figure 1**). Therefore, viscoelasticity must be paired with a nonlinear elastic component rather than a linear elastic one.

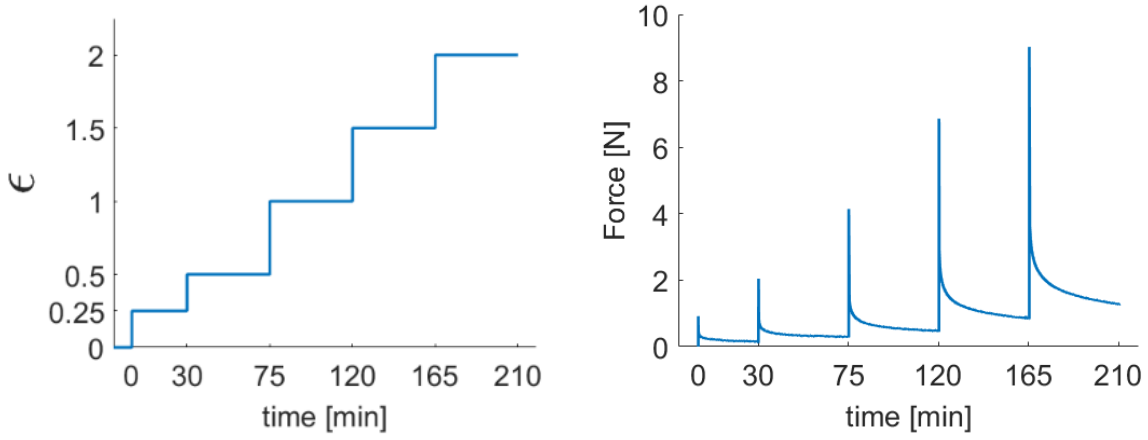

Figure 1. Nonlinear viscoelasticity during incremental stress-relaxation experiment

In the remaining sections of Chapter 1 I will introduce the mathematical framework that has been used in the past to study both elastic and viscoelastic behaviors of soft biological tissues. First, I will briefly discuss hyperelastic models and biphasic models, then I will focus in greater detail on discussing viscoelastic models, as it was the focus of parameter characterization difficulties.

1.2.1. Continuum Mechanics

In the continuum mechanics framework, one can use the deformation gradient tensor, F_{iA}, to represent the displacement from the reference configuration (undeformed) to the current configuration (deformed). The location of each particle in the reference and current configurations are described the position vectors X_A (material description) and x_i (spatial description), respectively (**Figure 2**). The displacement vector $\boldsymbol{u}$ is the difference between the two: $\boldsymbol{u} = \boldsymbol{x} - \boldsymbol{X}$.

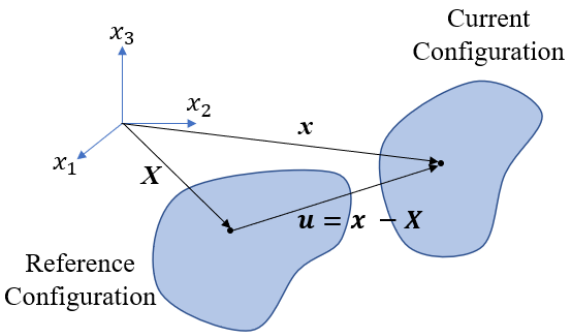

Figure 2. Reference (undeformed, material) configuration is transformed to current (deformed, spatial) configuration

The deformation tensor relates the material and spatial coordinates, and is defined as:

$$F_{i,A} = \frac{\partial x_i}{\partial X_A} \text{ or } \boldsymbol{F} = \frac{\partial \boldsymbol{x}}{\partial \boldsymbol{X}}. \tag{1}$$

From the deformation tensor, one can evaluate the right Cauchy-Green deformation tensor ($\boldsymbol{C}$, material description) and the left Cauchy- Green deformation tensor ($\boldsymbol{b}$, spatial description), as:

$$\boldsymbol{C} = \boldsymbol{F}^T\boldsymbol{F}, \tag{2}$$

$$\boldsymbol{b} = \boldsymbol{F}\boldsymbol{F}^T. \tag{3}$$

Furthermore, one can identify two commonly used two strain tensors, such as the Green-Lagrange tensor ($\boldsymbol{E}$, material description) and the Alamansi strain tensor ($\boldsymbol{e}$, spatial description) defined as:

$$\boldsymbol{E} = \frac{1}{2}(\boldsymbol{C} - \boldsymbol{I}), \tag{4}$$

$$\boldsymbol{e} = \frac{1}{2}(\boldsymbol{I} - \boldsymbol{b}^{-1}), \tag{5}$$

where $\boldsymbol{I}$ is the identity matrix. The deformation metrics described above are used in many constitutive equations, such as neo-Hookean material description, Donnan equilibrium model, and quasi-linear viscoelasticity.

1.2.2. Hyperelasticity

Soft biological tissues have nonlinear relationships between stress and deformation and often undergo large deformations; for these reasons they require more sophisticated constitutive equations than linear elasticity to describe their behavior. There is no consensus on the best hyperelastic model to describe the pseudo-static behavior of the urinary bladder; in our study we first employed the neo-Hookean hyperelasticity, in order to reduce the number of variables. **Table 1** compares this model with linear elasticity (Hooke's law), where $J = \det(\boldsymbol{F})$ and λ and μ are the Lamé parameters defined as:

$$\lambda = \frac{vE}{(1+v)(1-2v)}\,, \tag{6}$$

$$\mu = \frac{E}{2(1+v)}\,, \tag{7}$$

where E and v are Young's Modulus and Poisson's Ratio, respectively.

Material	Cauchy Stress
Linear Elasticity	$\boldsymbol{\sigma} = \lambda \mathrm{tr}\boldsymbol{\varepsilon}(\boldsymbol{I}) + 2\mu\boldsymbol{\varepsilon}$, where $\boldsymbol{\varepsilon} = \frac{1}{2}\left(\frac{\partial \boldsymbol{u}}{\partial \boldsymbol{x}} + \left(\frac{\partial \boldsymbol{u}}{\partial \boldsymbol{x}}\right)^T\right)$
Neo-Hookean Hyperelasticity	$\boldsymbol{\sigma} = \frac{\mu}{J}(\boldsymbol{b} - \boldsymbol{I}) + \frac{\lambda}{J}(\ln J)\boldsymbol{I}$

Table 1. Comparison of the Cauchy stress functions for Neo-Hookean elastic versus Neo-Hookean hyperelastic materials as defined in the FEBio software (Maas et al., 2011)

1.2.3. Donnan Equilibrium Biphasic Model

There are multiple approaches to modelling swelling of tissues in an aqueous solution. In the FE software FEBio, for example, users can opt to use biphasic-solute, biphasic, triphasic or multiphasic theory, and combine these with different types of solutions, porosity, and material models. The biphasic model describes a mixture of a porous permeable solid and interstitial fluid (Maas et al., 2011). To model a triphasic material with the Donnan equilibrium model of swelling, one assumes that a negative charge

gradient between the solution and the solid prompts movement of fluid into or out of the porous solid, resulting in swelling or shrinking of the tissue. The inputs of the model are the bath osmolarity, as well as elastic properties, the volume fraction, and the fixed charge density of the porous media. The effective stress of the mixture is a combination of elastic stress $\boldsymbol{\sigma}^e$ and fluid pressure p:

$$\boldsymbol{\sigma} = -p\boldsymbol{I} + \boldsymbol{\sigma}^e, \tag{8}$$

where the fluid pressure p is defined as:

$$p = R\theta\left(\sqrt{\left(\frac{1-\varphi_r^s}{J-\varphi_r^s}c_r^F\right)^2 + (\bar{c}^*)^2} - \bar{c}^*\right). \tag{9}$$

The constants introduced in **Eq. 9** are dependent on the properties of the solid, fluid, and surroundings, and are specified in **Table 2**.

R	8.3145 [$\mathrm{J \cdot mol^{-1} \cdot K^{-1}}$] (The universal gas constant)
θ	The temperature of the bath [K]
φ_r^s	Volume fraction of the solid in the reference configuration
c_r^F	Fixed charge density [$C \cdot \mathrm{m^{-3}}$] in the reference configuration, related to fixed charge density in the current configuration c^F by: $c^F = \frac{1-\varphi_r^s}{J-\varphi_r^s}c_r^F$
$\bar{c}^*$	Bath osmolarity [Osm], related to bath concentration c^*[Osm/L] by: $\bar{c}^* = 2c^*$

Table 2. Constants used in the Donnan equilibrium model of swelling used in FEBio (Maas et al., 2011)

1.3. Viscoelasticity

The focus of this thesis is to identify an accurate model to describe the viscoelastic properties of the UB wall. Mathematical models that describe viscoelasticity derive from mechanical spring-dashpot models. The three basic linear viscoelastic models found in literature are the Voigt/Kelvin model, the Maxwell model, and the Standard Linear Solid (SLS), pictured in **Figure 3**.

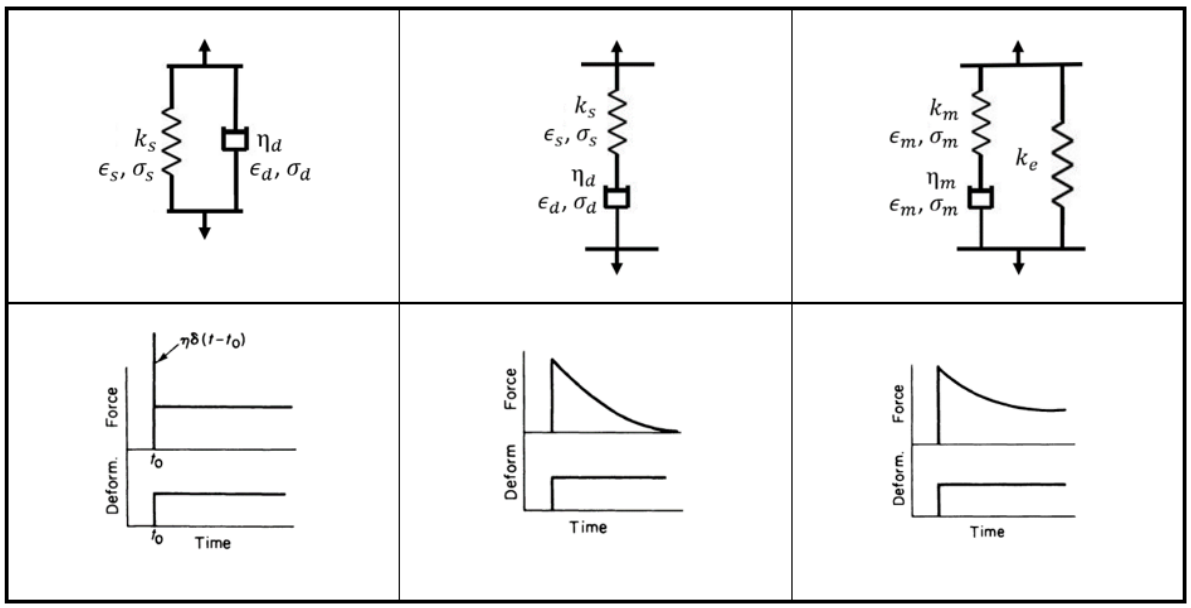

Figure 3. Voigt/Kelvin model (spring and dashpot in parallel), the Maxwell model (spring and dashpot in series), and the Standard Linear Solid (SLS) (spring and Maxwell element in parallel) [Vincent, 2012] and their corresponding stress response to step strain [Fung, 1981]

1.3.1. The Weichert Model

Complex arrangements of elements of springs and dashpots in series or parallel (known as lumped parameter models) have been explored by Tschoegl (1989). However, literature suggests that the Weichert model (also called generalized Maxwell model) is acceptable for material characterization of viscoelastic soft tissues [Vincent, 2010]. This model is composed of a single spring element and n Maxwell elements in parallel (**Figure 4**).

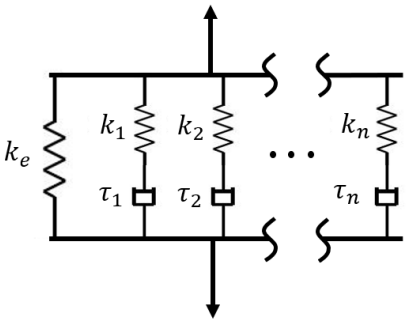

Figure 4. Weichert model schematic, composed of one spring element and n Maxwell elements in parallel

The Maxwell model is developed under the following assumptions:

$$\sigma = \sigma_s = \sigma_d, \tag{10}$$

$$\epsilon = \epsilon_s + \epsilon_d. \tag{11}$$

Where $\sigma_s, \sigma_d, \epsilon_s, \epsilon_d$ are from **Figure 3**. The strain and strain rate generate stresses in the spring and in the dashpot elements, respectively, following the laws:

$$\sigma_s = k\epsilon, \tag{12}$$

$$\sigma_d = \eta\dot{\epsilon}, \tag{13}$$

where k is stiffness $[N/m^2]$ and η is viscosity $[N \cdot s/m^2]$. Combining equations (10) – (13) one can calculate a relationship between strain rate, and stress and stress rate, as:

$$\dot{\epsilon} = \dot{\epsilon}_s + \dot{\epsilon}_d = \frac{\dot{\sigma}}{k} + \frac{\sigma}{\eta}. \tag{14}$$

Finally, defining the time constant as $\tau = \eta/k$ and rearranging equation (14), we can ultimately derive the differential equation for stress:

$$\sigma = \eta\dot{\epsilon} - \tau\dot{\sigma}. \tag{15}$$

When this model is applied to a stress relaxation test, strain rate is assumed to be 0 after applying the stress. Inserting $\dot{\epsilon} = 0$ and integrating, the final time dependent stress can be written as:

$$\sigma(t) = \sigma_0 \exp\left(-{}^{t}/_{\tau}\right). \tag{16}$$

From **Eq. (16)** it can be seen that for the Maxwell model when $t \to \infty$, the stress goes to zero. However, soft tissues do not relax to a stress equal to zero when $t \to \infty$, but they relax to a value of stress dependent on the applied strain. This is why the Maxwell model is combined in parallel with a simple spring in the SLS model. It is easiest to derive the SLS stress-strain relationship from the Laplace transform of **Equations (12)** and **(16)**, where $L[\dot{\sigma}] = s\tilde{\sigma}$. The stress of the Maxwell and spring elements, respectively, are then:

$$\tilde{\sigma}_m = \frac{k_m s}{\frac{1}{\tau_m} + s}\tilde{\epsilon}, \tag{17}$$

$$\tilde{\sigma}_s = k_e \tilde{\epsilon}\,. \tag{18}$$

Using the assumption that $\sigma = \sigma_s + \sum_n \sigma_n \Rightarrow \tilde{\sigma} = \tilde{\sigma}_s + \sum_n \tilde{\sigma}_n$, the stress in the Laplace space can be written as:

$$\tilde{\sigma} = \left(k_e + \sum_n \frac{k_n s}{\frac{1}{\tau_n} + s} \right) \tilde{\epsilon} = \Sigma \tilde{\epsilon}, \tag{19}$$

where $\Sigma = k_e + \sum_n \frac{k_n s}{\frac{1}{\tau_n} + s}$ is the time dependent "relative modulus" in the Laplace space. For a stress-relaxation test, strain is zero until time $t = t_n$ and can be represented by the Heaviside function. For $t_n = 0$, we have that:

$$\epsilon(t) = \epsilon_0 u(t) \Rightarrow \tilde{\epsilon}(s) = \frac{\epsilon_0}{s}. \tag{20}$$

Inserting this expression for strain into **Eq. (19)** and taking the inverse Laplace $\sigma(t) = L^{-1}[\Sigma \tilde{\epsilon}]$ yields the final stress-strain relationship for the Weichert Model, with n Maxwell elements, as:

$$\sigma(t) = \left(k_e + \sum_n k_n \exp\left(-{}^{t}/_{\tau_n}\right) \right) * \epsilon_0\,. \tag{21}$$

In **Eq. (21)** k_n and τ_n are referred to as the relaxation strengths and relaxation times, respectively; k_e is representative of the modulus of elasticity of the elastic (spring) element; and $\sum_n k_n \exp\left(-{}^{t}/_{\tau_n}\right)$ is the relaxation function that defines the discrete spectra in pairs k_n, τ_n. The summation in **Eq. (21)** is also referred to as the Prony Series. A visual representation of how each component of the series contributes to the overall behavior is seen in **Figure 5**.

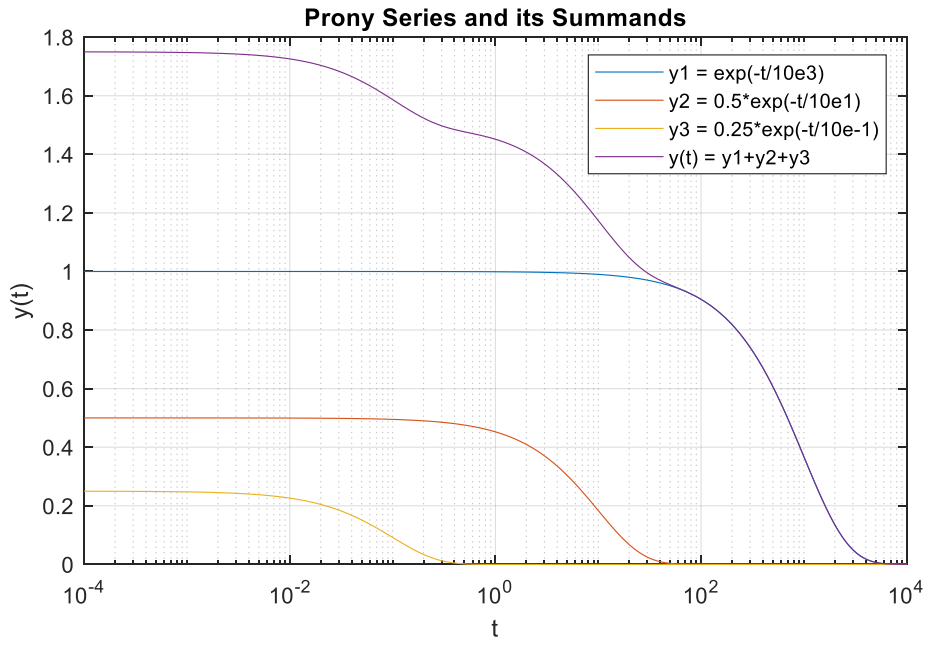

Figure 5. An example Prony Series on the logarithmic scale shows the decay of each component and contribution to initial value at $y(0)$

1.3.2. Linear Viscoelasticity

The Weichert Model is a good starting point for understanding the derivation of viscoelastic models but is usually applied only to 1D uniaxial tension tests. Additionally, derivation of the stress-strain relationship from the Laplace domain to time domain requires knowing the strain history, therefore, a general model of viscoelasticity applicable to stress and strain tensors with any strain history is desired.

A one-dimensional case of a simple bar elongated by $\epsilon(\tau)$ and experiencing stress $\sigma(t)$ is considered. All the lengthening history due to $\epsilon(\tau)$ is considered up until time *t*. For a small time-interval τ , the elongation increment is $\frac{d\epsilon(\tau)}{d\tau}d\tau$ and causes a stress $d\sigma(t)$. The elongation and stress increments are related to each other via the proportionality constant G which is a function of the time interval $(t - \tau)$ as:

$$d\sigma(t) = G(t - \tau)\frac{d\epsilon(\tau)}{d\tau}d\tau. \tag{22}$$

It follows that we can estimate the entire loading history by integrating **Eq. (22)** and obtaining:

$$\sigma(t) = \int_{-\infty}^{t} G(t - \tau) \frac{d\epsilon(\tau)}{d\tau} d\tau, \tag{23}$$

where $G(t)$ is the relaxation function. If $G(t)$ is assumed to be a tensor of material characteristics, then the stress-strain relationship in **Eq. (23)** can be written as a constitutive equation, with σ_{ij} and ϵ_{ij} as function of space and time, and G_{ijkl} being the tensorial relaxation function:

$$\sigma_{ij}(\boldsymbol{x}, t) = \int_{-\infty}^{t} G_{ijkl}(\boldsymbol{x}, t - \tau) \frac{\partial \epsilon_{kl}}{\partial \tau}(\boldsymbol{x}, \tau)\, d\tau. \tag{24}$$

If motion begins at $t = 0$, and $\sigma_{ij} = \epsilon_{ij} = 0$ for $t < 0$, then Eq. (24) becomes

$$\sigma_{ij}(\boldsymbol{x}, t) = G_{ijkl}(\boldsymbol{x}, t)\epsilon_{kl}(\boldsymbol{x}, 0^{+}) + \int_{0}^{t} G_{ijkl}(\boldsymbol{x}, t - \tau) \frac{\partial \epsilon_{kl}}{\partial \tau}(\boldsymbol{x}, \tau)\, d\tau. \tag{25}$$

A viscoelastic solid that behaves following the law described in **Eq. (25)** is said to be linear viscoelastic. However, tissues have nonlinear stress-strain relationships and so Fung (1981) developed a different viscoelastic function. In continuum mechanics, the QLV model has broader applications because it can be used with most experimental data sets such as stress relaxation, creep, and hysteresis [Fung, 1981]. QLV theory has been applied in finite element software, including the viscoelastic model found in FEBio [Maas et al., 2011].

1.3.3. Quasilinear Viscoelasticity (QLV)

Consider a cylindrical specimen undergoing an infinitesimal change in stretch λ where the stress response K is assumed to be a function of time *t* and stretch λ. The stress response denoted as $K(\lambda, t)$, is also known as the relaxation function and is defined as:

$$K(\lambda, t) = G(t)T^{(e)}(\lambda), \qquad G(0) = 1, \tag{26}$$

where $G(t)$ is the reduced relaxation function (dimensionless) and $T^{(e)}(\lambda)$ is the elastic response (dimension of a stress). The stress response for an instant of time τ where $t > \tau$ can be evaluated as:

$$G(t-\tau)\frac{\partial T^{(e)}[\lambda(\tau)]}{\partial \lambda}\delta\lambda(\tau). \tag{27}$$

It follows, that the stress at any time *t*, which is depending on the entire stress history, can be evaluated from **Eq. (26)** as:

$$T(t) = \int_{-\infty}^{t} G(t-\tau)\frac{\partial T^{(e)}[\lambda(\tau)]}{\partial \lambda}\frac{\partial \lambda(\tau)}{\partial \tau}d\tau. \tag{28}$$

Again, the strain is assumed to be applied at $t = 0$, as well $T = 0$ and $\lambda = 1$ for $t \leq 0$, which allows us to evaluate:

$$T(t) = T^{(e)}(0^+)G(t) + \int_{0}^{t} G(t-\tau)\frac{\partial T^{(e)}[\lambda(\tau)]}{\partial \tau}d\tau, \tag{29}$$

which can be generalized in a 3-dimensional constitutive equation as:

$$T_{ij}(t) = T_{kl}^{(e)}(0^+)G_{ijkl}(t) + \int_{0}^{t} G_{ijkl}(t-\tau)\frac{\partial T_{kl}^{(e)}[\boldsymbol{E}(\tau)]}{\partial \tau}d\tau, \tag{30}$$

where $T_{ij}(t)$ is the Kirchhoff stress tensor, E_{ij} is the Green's strain tensor, and $G_{ijkl}(t)$ is the reduced relaxation function tensor. "Reduced" refers to the condition that $G_{ijkl}(0) = 1$, or that the function is nondimensional. This function resembles **Eq. (25)** except for the elastic stress can be derived from any hyperelastic or elastic material.

1.3.4. The Reduced Relaxation Function

At $t = 0$ we assume that $G(0) = 1$. This is accomplished with the normalization of the relaxation spectrum by:

$$G(t) = \frac{\sum \gamma_i e^{-t/\tau_i}}{\sum \gamma_i}. \tag{31}$$

The purpose of normalizing the relaxation spectrum is so that the relaxation parameters can be studied separate from elastic parameters. The condition $G(0) = 1$ implies that $\sum \gamma_i = 1$. This holds true for

normalized data, but it should be noted that in the Weichert model, γ_i do not sum to 1 because they are analogous to Young's Modulus (spring constants for each Maxwell component). For QLV theory, Fung derived a generalized reduced relaxation function compatible with continuous spectrums:

$$G(t) = \frac{1 + \int_0^\infty S(\tau)e^{-t/\tau}d\tau}{1 + \int_0^\infty S(\tau)d\tau}. \tag{32}$$

The spectrum $S(\tau)$ considers the variable τ to be continuous from 0 to ∞. The relative amplitude (relaxation strengths in a discrete spectrum) is a function of τ (see **Figure 6**). The generalized QLV model (**Eq. 30**) can use either a **discrete relaxation spectrum (DRS)** or a **continuous relaxation spectrum (CRS)** where a DRS is a sum of discrete spectra pairs and the CRS takes the form of an integrable function of τ.

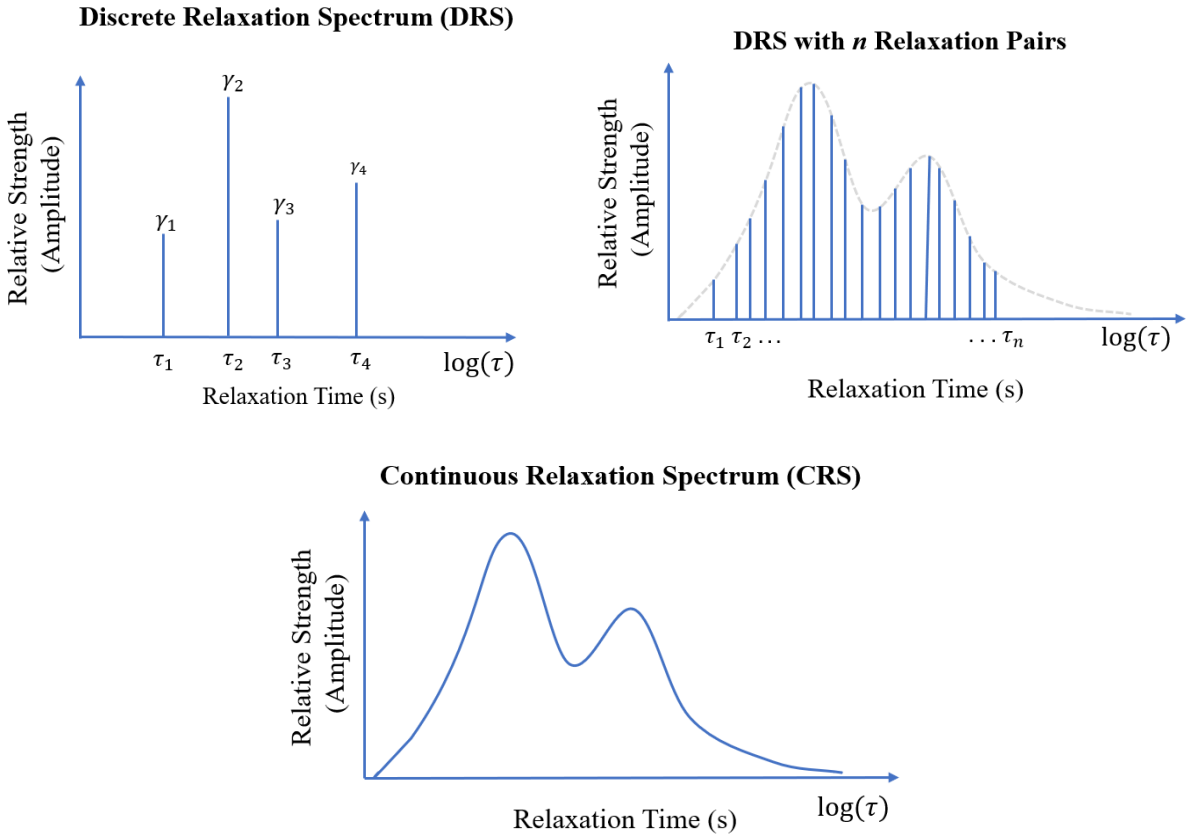

Figure 6. Visual representation of discrete spectrum of relaxation constants (top left) and how a relatively infinite spectrum of relation constants (top right) can be represented by a continuous spectrum (bottom)

1.3.5. Advantages and Disadvantages to DRS and CRS

The same reduced relaxation function can often be represented equally satisfactorily by both CRS and DRS as seen in **Figure 7**. However, they each come with benefits and downsides. Choosing which one is best can depend on the application.

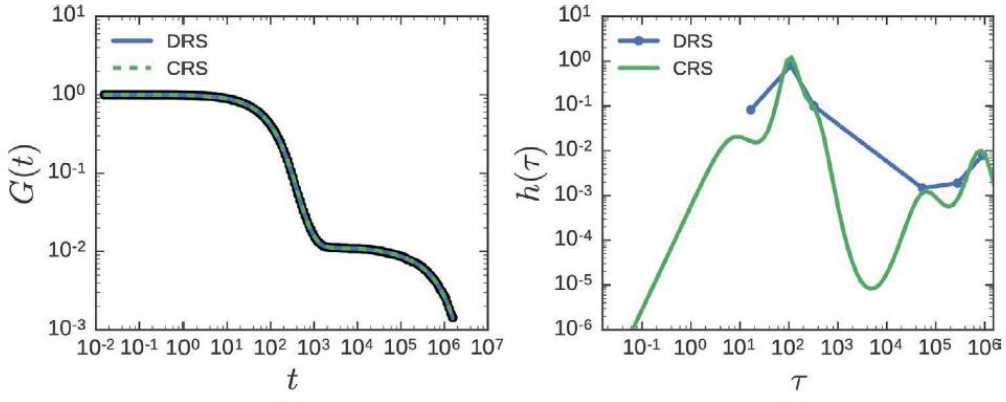

Figure 7. An example of a DRS and CRS representing the same reduced relaxation function of time where $\frac{h(\tau)}{\tau} = \sum_{i=1}^{n} \gamma_i \delta(\tau - \tau_i)$ [Shanbhag, 2019]

DRS are often used because of their computational efficiency [Park and Kim, 2001]. The equation is straightforward: it is the sum of exponential functions, referred to as the Prony Series in many papers. Unfortunately, the Prony series is an ill-posed problem, meaning it does not have a unique solution [Baumgaertel and Winter, 1989] [McDougall et al., 2014]. In other words, a single relaxation curve can be represented by multiple combinations of relaxation spectra [Fung, 2013]. Additionally, DRS can include as many exponentials as desired for a well-fit curve, adding difficulty to the model selection because the user must define *n*, the number of viscoelastic pairs. For example, Liu, Z., and K. Yeung (2008) used an RRF composed of three sets of exponentials, resulting in eight total parameters to be optimized to describe their experimental data. On the one hand, while increasing the order of the Prony Series will decrease the apparent fitting error, it will also increase the "ill-posedness" [Baumgaertel and Winter, 1989]. On the other hand, a lower order Prony Series will decrease the uncertainty but might increase the error between theory and experiments.

A CRS combats this by reducing the number of variables. A CRS can reveal useful information about the relaxation behavior of constituents, as seen in the work of Nagatomi et al. (2008). Recent works have emphasized the need for rheologists to include CRS in their results [McDougall et al., 2104] and others have opted to only use them in their analyses of soft tissues [Nagatomi et al., 2004] [Nagatomi et al., 2008]. CRS can require as few as 3 variables to define the RRF, depending on the spectrum chosen. Although it reduces uncertainty, CRS are more difficult to implement because they involve integration. As a result of its computational expense, CRS are left out of viscoelastic models available in popular FE software.

2. LITERATURE REVIEW

2.1 Urinary Bladder Physiology and Tissue Properties

The UB is a multi-layered storage organ that undergoes large deformations multiple times a day, throughout the filling and voiding cycles. The urinary bladder wall (UBW) has complex mechanical behavior, that can be considered hyperelastic, in certain loading conditions, and viscoelastic (time dependent), in others. Sudden increases in volume due to fluid entering the bladder rapidly increase the pressure followed by a phase of viscoelastic relaxation until reaching a steady state again [Nagatomi et al., 2004]. The mechanical properties of this organ are crucial to its function, indeed a change in the pressure-volume relationship of the wall due to disease can significantly alter the UB function. Furthermore, disease and injury can cause remodeling of the UBW's microstructure and composition, which can result in altered geometry, compliance, contractility, and elasticity. A study on fetal bladder outlet obstruction (BOO), for example, found that obstructed bladders exhibited increased compliance and decreased elasticity and viscoelasticity [Thiruchelvam et al., 2003]. Likewise, contractile abnormalities can cause outflow obstruction [Fry and Wagg, 1999].

It is generally accepted that, like for most soft biological tissues, the bladder's mechanical properties are tied to its physiology. Obstructed bladders exhibit collagen deposition and ultimately to increased stiffness, which indicates the importance of tissue composition and constituents' density in determining bladder compliance [Fry and Wagg, 1999]. Furthermore, the bladders collected from rats subjected to a spinal cord injury were found to have increased elastin density, which resulted in reduced stress relaxation behavior (retaining a higher stress for longer) and increased bladder compliance [Nagatomi et al., 2004]. Therefore, it is important to consider the physiology of the UB and contribution of its components to its function.

The urinary bladder wall is a complex structure that can be divided in four distinct layers, each with their own unique properties: mucosa, submucosa, detrusor muscle, and adventitia (**Figure 7**). The innermost layer of the UBW, called the mucosa, is a thin layer of epithelial cells, which gathers in folds when the

bladder is empty. Umbrella cells and a layer of glycosaminoglycans protect the rest of the UBW by blocking diffusion of urine from the lumen. The outermost layer, the adventitia, is a thin layer composed of connective tissues. The two thickest layers, the submucosa and detrusor muscle, bear most of the load during deformation and have been the focus of mechanical testing on the UBW.

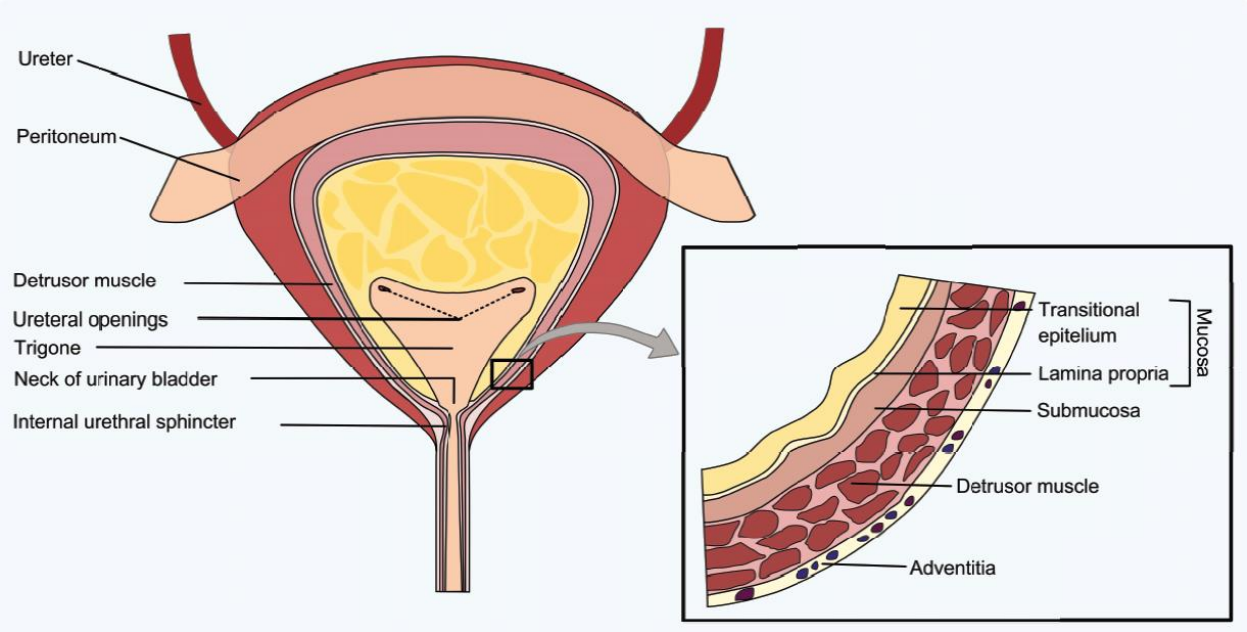

Figure 8. The geometry of the urinary bladder and layers of the urinary bladder wall [Roccabianca and Bush, 2016]

2.1.1. Submucosa

The submucosa is capable of large deformations, crucial to the filling phase, and consists mostly of extracellular matrix, that contains a network of collagen and elastin fibers. Elastin fibers provide compliance whereas collagen fibers provide strength. It is generally accepted that the interactions between fibers and the uncoiling and rearranging of fiber networks contribute to the mechanical behavior, both elastic and viscoelastic, of soft tissues [Shen et al., 2011] [Natali et al., 2015]. Overall, the ECM has observable viscoelastic properties, as seen in experiments performed on isolated ECM [Nagatomi et al., 2008].

2.1.2. Detrusor Muscle

The detrusor muscle mechanical function is to relax and distend during filling and perform active contractions during emptying. Smooth muscle cells contract causing an increase in urine's pressure, which then drives voiding. Contractility of the bladder smooth muscle cells (SMCs) is dependent on force generation within the muscle cells as well as viscous interactions with the ECM they reside in [Fry and Wagg, 1999]. Determining whether abnormalities in contractility are due to the muscle cells themselves or to changes in composition and structure of the ECM motivated Fry and Wagg to study isolated detrusor muscle in obstructed and healthy bladders [Fry and Wagg, 1999]. Obstructed bladders exhibit higher deposition of extracellular material compared to healthy bladders and offer a way to determine whether changes in the ECM are responsible for reduced compliance. They found no statistical difference in viscoelastic properties of the detrusor muscle in the passive state in healthy versus obstructed bladders. However, in the active state, viscoelastic properties were more apparent in the obstructed bladders than the healthy bladders. They speculated that this could be due to a smaller number of SMC's per unit mass because of deposition of ECM material.

2.1.3. Mechanical Properties Vary by Anatomical Location and Orientation

Multiple constituents and layers contribute to the macroscopically observed mechanical behavior in the UBW. It is difficult experimentally to separate the layers of the UBW, so often its mechanical properties are determined from bulk behavior of strips of the UBW containing all four layers. In this state, experimentalists can still observe anisotropy due to fiber orientation. Uniaxial tests over the years have shown that mechanical properties differ between strips in the longitudinal and transverse directions as well as between anatomical locations. Korossis et al. (2009) tested porcine urinary bladder strips in longitudinal and circumferential directions in 5 locations of the bladder: dorsal, trigone, lateral, ventral, and lower body (**Figure 8**). Uniaxial tests of the specimens were accompanied by histological characterization. They found that strips oriented longitudinally had higher stiffnesses than those oriented circumferentially. This is supported by their histological results which shows that the elastin fibers are oriented primarily in the

transverse direction. There were insignificant differences in anisotropy in the transverse direction by anatomical location, finding that is supported by the observed uniform expansion circumferentially during the filling phase.

Regional differences were significant as well. The dorsal and ventral regions had the highest compliance and least directional anisotropy. The lateral, lower body, and trigone regions had the highest tensile strengths, and the trigone region had the lowest failure strains along with the highest collagen phase slope, making it the least distensible region. In general, the basal regions (lower body and trigone) were less compliant than the apex regions (dorsal and ventral) and these properties were attributed to their collagen and elastin networks. From their results, it can be concluded that material anisotropy, elasticity, and viscoelasticity will vary based on harvest location.

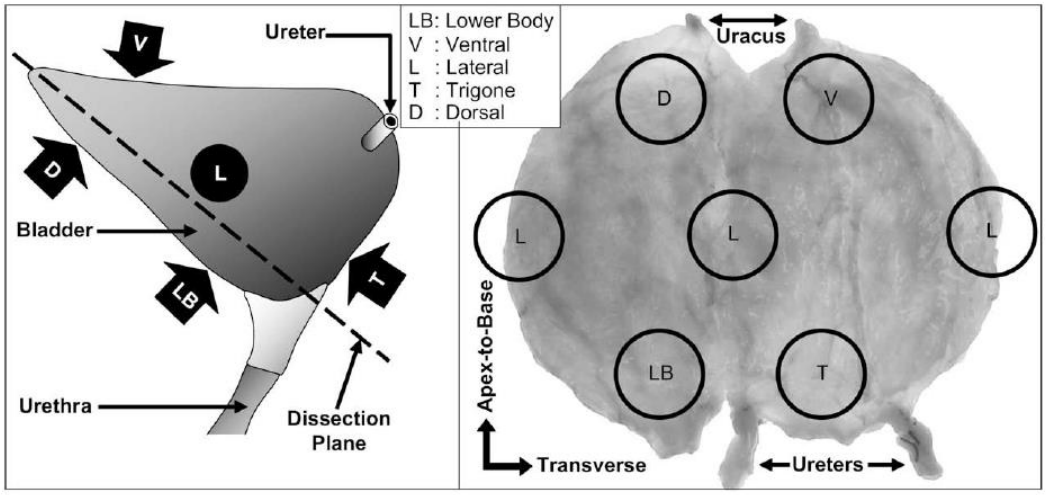

Figure 9. The dissection plane on porcine UB used by Korossis et al. (left) and the anatomical locations used in their experiment (right) [Korossis et al., 2009]

Other researchers focused on isolating constituents to observe their individual mechanical properties, as opposed to study the tissue intact. As mentioned previously, Fry and Wagg (1999) studied the detrusor muscle independent of the rest of the UBW by dissecting detrusor muscle strips and observed significant viscoelastic properties. Nagatomi et al. (2008) isolated the ECM through decellularization in order to determine a **reduced relaxation function (RRF)** (derived in **Section 1.3.4**). for the ECM independent of

the smooth muscles (SMs) (**Figure 9**). They used a dual Gaussian spectrum $S_{ECM}(\tau)$ (**Eq. 31**) where α_m, $log_{10}\mu_m$, $log_{10}\sigma_m$, are the amplitude, mean, and variance, respectively. Additionally, n is an integer that represents the total number of relaxation mechanisms are considered, and $n = 2$ was chosen to account the mechanical behavior of both collagen and elastin (see dotted lines in **Figure 9**). Results from a previous study on SMCs were used for a constant value continuous spectrum $S_{SM}(\tau)$ (**Eq. 32**), where τ_1 and τ_2 are the start and end of the spectrum respectively and c is the index representing the amount of overall relaxation and is dimensionless.

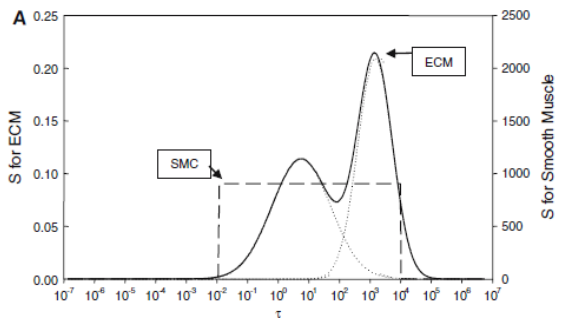

$$S_{ECM}(\tau) = \sum_{m=1}^{n} a_m \frac{\exp\left\{-\frac{1}{2}\left[\frac{(log_{10}\tau - log_{10}\mu_m)}{log_{10}\sigma_m}\right]^2\right\}}{log_{10}\sigma_m\sqrt{2\pi}} \quad (31)$$

$$S_{SM}(\tau) = \begin{cases} \frac{c}{\tau} & \text{for } \tau_1 \le \tau \le \tau_2 \\ 0 & \text{otherwise} \end{cases} \quad (32)$$

Figure 10. Relaxation spectrums of the ECM and SM [Nagatomi et al., 2008]

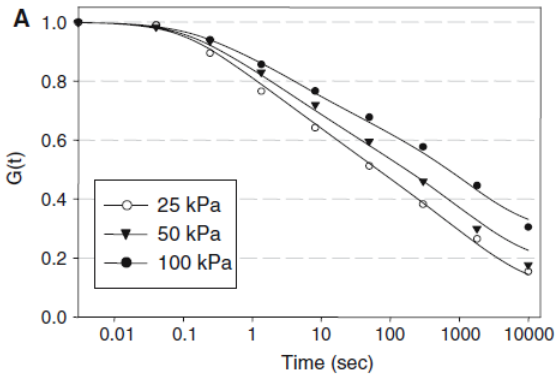

$$G(t) = \frac{1 + \int_0^\infty S(\tau)e^{-t/\tau}d\tau}{1 + \int_0^\infty S(\tau)d\tau} \quad (33)$$

$$G(t) = \phi_{ECM} * G_{ECM}(t) + \phi_{SM} * G_{SM}(t) \quad (34)$$

$$\phi_{ECM} = 1 - e^{-\beta P_0}, \ \phi_{SM} = e^{-\beta P_0} \quad (35)$$

Figure 11. The overall stress relaxation function $G(t)$ (left) determined by the equations on the right where β and P_0 are constants determined by optimization [Nagatomi et al., 2008]

The overall UBW reduced relaxation function $G(t)$ (**Fig. 10**, **Eq. 34**) was then modelled as the summation of each reduced relaxation function $G_{ECM}(t)$ and $G_{SM}(t)$ determined by **Eq. (33)** multiplied by their respective recruitment functions ϕ_{ECM} and ϕ_{SM} (**Eq. 35**). (The physical meaning and mathematical

description of the RRF and relaxation spectrums was detailed in **Section 1.3.4.**) These two studies demonstrate that mechanical properties vary between constituents.

While the exact contribution of individual components to viscoelasticity and hyperelasticity remains understudied, constitutive models are useful for predicting response to pathologies that influence geometry, composition, and therefore the capabilities of the bladder to void urine. Regardless of the type of constitutive equation chosen to describe the mechanical behavior, for the description of the tissue to be accurate the constitutive parameters must be informed by experimental data obtained from mechanical tests. This is usually achieved by an optimization process, via error minimization. In the following, we will first describe the mechanical tests that have been previously used to quantify the behavior of the UBW, and second the methods that have been used to fit models to experimental data. Here we focus on viscoelastic behavior.

2.2. Mechanical Tests

To study viscoelastic behavior of soft biological tissues, three common mechanical tests are employed: stress-relaxation, creep, and dynamic tests [Roylance, 2001] seen in **Figure 11**. Stress-relaxation tests are usually performed on a uniaxial or biaxial tensile machine and consist of applying an instantaneous strain to the sample followed by a relaxation time at constant strain. The stress-time curve will show a decrease in stress over time, hence “stress-relaxation”. Creep tests are set up the same as stress-relaxation tests, but aim to maintain a constant stress over time, rather than a constant strain, this results in an increase in strain over time. Finally, dynamic loading tests are performed by loading a tissue surface with an oscillatory load and quantifying the phase shift between applied stress and recorded strain. Uniaxial stress-relaxation experiments were performed in this work.

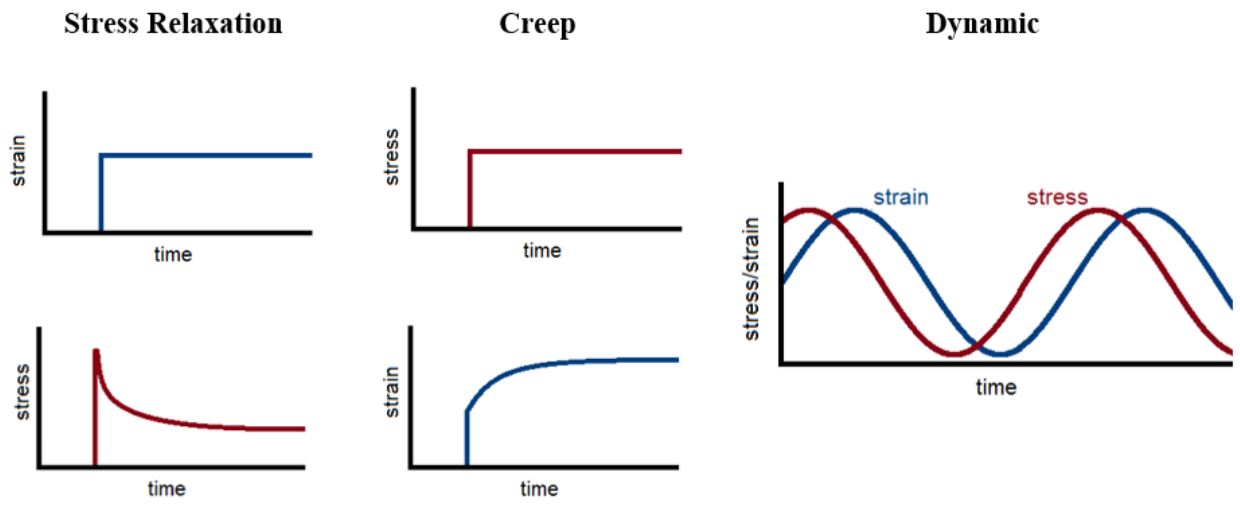

Figure 12. Stress and strain of three common mechanical tests from left to right: stress-relaxation, creep, and dynamic

2.3. Experimental Challenges

Replicating and comparing experimental results on the UB has presented many obstacles over the years. Results from studies often contradict each other. For example, two studies comparing the maximum stress of young versus older bladders found opposite relationships between age and stiffness. Martins et al. (2011) tested female cadavers for their maximum stress and found that the group of females age 50 years and older had lower stiffness compared to the group of females below 50 years of age; they concluded that bladder stiffness decreased with age. Chantereau et al. (2014), however, in a similar study on female cadavers found that bladders harvested from older individuals, with an average age of 75, had a higher stiffness compared to that of younger individual, with an average age of 29. Another set of studies found conflicting results about the anisotropy of the UBW. While one study found a larger stiffness in the longitudinal (apex to base) direction [Korossis et al., 2009], the other study found higher stiffness in circumferential (transverse) direction [Zanetti et al., 2012]. Details of these studies results and other UB experiments can be found in literature [Roccabianca and Bush, 2015]. These discrepancies could be due to a lack of standardized experimental protocol.

Studies often vary in strain rate, temperature, reference frame, and maximum strain applied (high strain >200% or lower strain <100%). Many tests are conducted at room temperature and temperature is known to affect viscoelasticity [Roylance, 2001]. Papers also fail to specify important factors about their samples, such as sex [Dahms et al., 1998]. Lastly, experimentalists are challenged with creating *ex vivo* environments that mimic as much as possible *in vivo* conditions. For example, hydration seems to greatly affect the elastic and viscoelastic behavior of the UBW, however, specimens are often tested at different levels of hydration. Many papers do not mention submerging their specimens in any solution [Chantereau et al., 2014], or they store samples in solution prior to testing but not during [Natali et al., 2015] [Dahms et al., 1998]. Others perform tests in modified Krebs solution [Nagatomi et al., 2004] [Nagatomi et al., 2008] [Van Mastrigt and Nagtegaal, 1981], Tyrode solution [Thiruchelvam et al., 2003] or saline solution [Korossis et al., 2009]. Furthermore, it has been suggested that viscoelasticity of tissues *in vivo* can be attributed, at least in part, to viscous interactions between cells and interstitial fluid [Natali et al., 2015]. The large variation between experimental approaches makes it crucial to question the validity of comparisons between studies.

For now, the findings indicate the complexity of modelling the UB based on a multitude of factors: geometry, regional differences, fiber orientation, constituents, and experimental approach. Multiphysics models might someday model multiple phenomena at once during the filling and voiding of the UB. Until then, it is important to isolate individual factors and study their effects on overall UB function to aid in the creation of computational models. In this study we focused on two factors of interest: the differences in viscoelastic behavior by anatomical region and by bath osmolarity during a swelling test. Work by Korossis et al. (2009) highlighted the inhomogeneity among anatomical region and direction of the bladder. From uniaxial quasi-static mechanical tests on porcine bladders, they found that the basal region of the UB around the neck of the urethra had higher stiffness than apical regions. To investigate viscoelastic behavior based on anatomical region and bath osmolarity, we must discuss the different viscoelastic models available. As discussed in **Section 1.3**, a discrete relaxation spectrum (DRS) or continuous relaxation spectrum (CRS) can be used. Choosing the best one can be difficult.

2.4. Challenges in Analytical Methods (Parameter Characterization)

Parameter characterization of viscoelastic materials can be split into two parts. The elastic parameters' portion of the constitutive equation can be determined by the equilibrium stress at the end of a stress relaxation curve. This correlates with the single spring element in the Weichert model (**Figure 4**). The relaxation spectra are more difficult to approximate.

For decades, researchers have tried to obtain "exact" relaxation spectra from experimental data with various optimization algorithms. The solution is not very straightforward due a few complications:

1) CRS and DRS are ill-posed problems meaning they do not have a unique solution. Optimization of spectra might arrive at false minima before finding the best fit spectra [Doehring et al., 2004].
2) CRS and DRS are very sensitive to noise in the data [McDougall et al., 2014]
3) DRS optimized without constraints can give negative parameters that have no physiological meaning [McDougall et al., 2014]
4) QLV does not account for strain-rate dependence in large deformations [Fung, 1981]

Of the first attempts to fit exact relaxation spectra, Schapery (1962) fit parameters using a simple collocation method. To improve the accuracy of this method, Cost and Becker (1970) developed a "multidata" method but failed to prevent negative coefficients. To tackle negative parameters, later methods attempted interactive adjustment of parameters, recursive algorithms, regularization, and quadratic programming [Park and Kim, 2001]. Simpler approaches have involved pre-smoothing noisy data with a power series [Park and Kim, 2001]. Detailed discussion of these techniques in terms of computational efficiency, mathematical background, and implementation are readily available in literature [Park and Schapery, 1999] [Park and Kim, 2001] [Shanbhag, 2019] [McDougall et al., 2014]. And so, while issues (1), (2), and (3) are solved by these methods, they are relatively inaccessible. While many have published papers of their work fitting CRS, very few have shared their codes online, as pointed out by Shanbhag and McDougall et al. in their works [Shanbhag, 2019] [McDougall et al., 2014]. End-users of these codes are likely to be unfamiliar

with mathematical concepts presented in literature making it difficult to reproduce code independently. Recently, computational physicists have created open-source codes for rheologists such as "pyReSpect" [Shanbhag, 2019].

To address strain-rate dependence, issue (4), QLV has been altered on a few occasions in literature [Van Mastrigt and Nagtegaal, 1981]. Abramowitch and Woo (2004) developed a piecewise constitutive equation to simultaneously fit the ramping and relaxation phases. It was shown to improve the fitting of experimental data sets in comparison with QLV theory alone. Furthermore, more complications arise depending on the form of stress-strain data and comparisons one wishes to make between the data sets. Finally, these methods have not been applied to 3D constitutive equations, to our knowledge. The major concerns are then:

5) CRS cannot be used to simulate tissues and organs in FE
6) Algorithms available online do not fit data from multi-step strains and each stress-strain curve must be analyzed independently QLV requires normalizing stress data to the peak stress
7) Inter-parameter sensitivity (see **Figure 13**) makes it difficult to compare fitted data among samples differing in pathology

Our research aims to fit data to 5 incremental strains resulting in a series of stress-relaxation curves (**Figure 1**). Additionally, we hypothesize based on work by Korossis et al. (2009) that there may be differences in viscoelastic parameters based on anatomical locations. Therefore, we must be able to compare parameters between the data sets. Implementing these models in FEBio is the final goal.

2.4.1. Intercorrelation Algorithms

A solution to the issue (5) has been addressed by intercorrelation algorithms that solve for the CRS and create DRS based on the CRS. Intercorrelation was successfully used by Labus et al. (2016) to model brain tissue by using peaks in the CRS to define the best discrete relaxation times. Also, Mun and Goangseup (2010) used an intercorrelation method to fit 16 pairs of relaxation constants to CRS obtained from dynamic

tests on asphalt concrete. The “pyResPect” algorithm mentioned earlier also uses an intercorrelation technique to solve for the DRS based on CRS.

2.4.2. Lack of Incremental Curve Fits

It is standard practice to fit elastic parameters to raw stress data, normalize the stress data, then fit viscoelastic parameters to the normalized stress. This method separates elastic and viscoelastic parameters, which are meant to be dimensionless [Sarver et al., 2003]. This works well for single stress relaxation curves but was rarely applied to incremental stress-relaxation curves for experiments with sequential strain increases. Incremental strain increases can be difficult to model due to the “strain memory” of UB tissue. The stress state of the tissue is dependent on all previously applied loads.

Many papers avoid fitting incremental tests by only ramping their samples once. Liu and Yeung (2008) fit their parameters to normalized stress curves of strains of 5%, 10%, and 15% separately. The highest strain 15% had the lowest relaxed normalized stress. This is contradictory to our raw data where incrementally larger strains were applied to samples and larger strains produced larger relaxed stresses. Sarver et al. (2003) comment on this relationship between strain and relaxation; they note that common normalization techniques are dependent on equilibrium stress, which is dependent on strain, violating “strain independence” of QLV. Sarver et al. (2003) derive an expression for stress relaxation based on incremental strains using a non-strain dependent normalization method, solving issue (6). Unfortunately, this expression differs from constitutive equations used in FE software such as FEBio, so parameters optimized will not transfer to 3D simulations.

2.4.3. Inter-parameter Sensitivity as Motivation for Constant Relaxation Times

For situations where only discrete relaxation spectra can be used, such as in FE simulations, caution is advised for parameter comparisons of bladders with different pathology. One may fit relaxation strengths and relaxation times to separate sets of data, but it is not wise to draw correlations between the relaxation strengths if the relaxation times are different. The relaxation strengths are coefficients to the exponential,

which is dependent on the relaxation time. To demonstrate this, a Prony Series (**Eq. 21**) of 3 exponentials was fit to stress relaxation data from a single strain from our experiments using the time constants $\tau_1 = 0.16$, $\tau_2 = 7$ and a range of τ_3 from 10^1 to $10^{3.5}$. The resulting values of E_3 change every time τ_3 is increased (**Figure 13**). The entire Prony Series is a summation of all relaxation pairs so any change to E_3 will require a change to E_1 and E_2 as well (**Figure 13**).

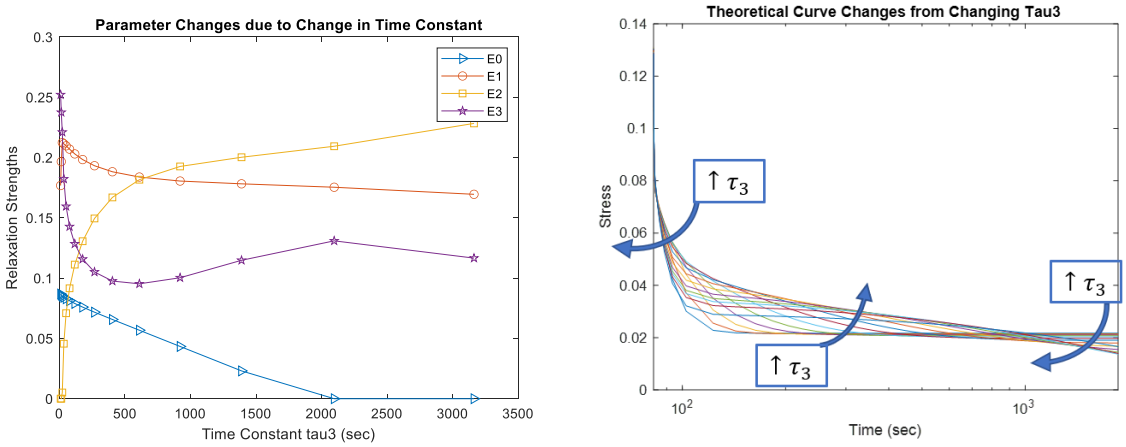

Figure 13. Inter-dependence of relaxation strength and relaxation time where $E_0, E_1, E_2, and\ E_3$ (corresponding to $k_0, k_1, k_2, and\ k_3$ in **Eq. (21)**) change values when optimized to a new time constant τ_3

Additionally, the DRS represented by a Prony series has sensitivity to different parameters at different location along the curve (see **Figure 5**). Simple least squares optimization is inefficient because they do not account for parameter relationships.

This is likely why many choose to set their relaxation times as constants and optimize the relaxation strengths. [Goh et al., 2004] fit between two to five relaxation strengths to nonlinear elastic polynomial and Ogden models. Abramowitch and Woo (2004) fit their piecewise model using three set time constants using the Levenberg-Marquardt approach to minimize their function. This is the best way to fit time constants with certainty in results if using a least-squares minimization approach. The downside to this method is that the investigator must determine the best time constants and best number of time constants heuristically, introducing human bias.

More methodical approaches avoid user bias by using machine learning instead of setting the relaxation times as constants. The potential usefulness of machine learning is that it can solve ill-posed problems like the Prony Series without user-bias. Genetic algorithms are a subset of machine learning techniques inspired from the Darwinian principle of survival of the fittest [Kohandel, 2008]. The algorithm begins with a "population" of *n* possible solutions and allows them to progress to the next evolution phase if they are best fit compared to their competitors. Kohandel (2008) used a genetic algorithm to fit both relaxation strengths and relaxation times to the alternative QLV constitutive equation developed by Abramowitch and Woo (2004). A genetic algorithm is available in MATLAB that considers relationships between parameters. This can be used to create constraints between variables using inequalities.

2.4.4. Method Selection

In conclusion, there exists algorithms developed over decades to fit exact relaxation spectra for DRS and CRS alike. These are incredibly useful for studying the relaxation behavior of soft tissues through a single step strain test. These algorithms are likely to aid in identifying underlying mechanisms of relaxation in tissues in uniaxial stress-relaxation tests. If the only desire is to simulate bladder behavior in FE software such as for patient specific modelling from cystography, CRS conversion to DRS is a suitable option.

In the case where relaxation behavior is to be compared between data sets rather than averaged from all tests, it is advisable to set relaxation times for the DRS to avoid fitting parameters that are not actually comparable. A methodical approach for fitting relaxation strengths to set relaxation times will speed up analysis since sensitivity of the relaxation constants along the curve vary. Fitting a continuous relaxation spectrum is also useful for comparison of these data sets but should not be converted to DRS because those will likely yield different relaxation times, leaving the parameters incomparable.

For complex strain histories, researchers might need to replicate models such as those by Abramowitch and Woo (2004) and Sarver et al. (2003) or use FEBio recognizing that time dependent and elastic components are inseparable for analysis. Parameters from the former method are not transferable to the latter method.

If FE simulation of complex strain histories are desired for comparison of data sets, as in our case, the user must set their relaxation times if they hope to find statistically significant differences among parameters. Methodical parameter optimization will also be useful in this situation.

3. MODELLING OF URINARY BLADDER TISSUE

3.1 Introduction

We hypothesize that mechanical properties of the urinary bladder differ between anatomical locations based on the findings of Korossis et al. (2009) and that the stress state of tissues samples is different in solutions of varying osmolarity. To test this theory, we performed uniaxial tests on porcine UB strips. Our data is in the form of 5 incremental stress relaxation curves. An outline of the experimental set up is first presented followed by each model that was tested. The bulk of the analytical work for this data was in finding a suitable viscoelastic constitutive model to fit the data with. To make intentions for each model clear, the methods, results, and discussion will be presented for each model before moving on to the next model.

Four models were explored. The first two fit elastic and viscoelastic parameters: (1) Quasilinear viscoelasticity using a discrete relaxation spectrum (DRS) (**Figure 6** and **Sections 1.3.3., 1.3.4.**) and (2) the Weichert Model (**Figure 4** and **Section 1.3.1.)** using a continuous relaxation spectrum (CRS) (**Figure 6** and **Section 1.3.4.**) in place of a series of infinite Maxwell elements. The last two models only fit the viscoelastic parameters by fitting a reduced relaxation function (RRF) (**Eq. 32** and **Section 1.3.4.**) to normalized data. These models were (3) RRF using a CRS defined by **Eq. 31** with n=1 and (4) RRF using a CRS defined by **Eq. 31** with n=2. Advantages and disadvantages for each model will be discussed as well as future work that will improve on the results presented.

3.2. Experimental Methods

The following experiment was performed by Tyler Tuttle, a fellow lab member of EMBR Lab and Mechanical Engineering PhD candidate at Michigan State University.

Porcine urinary bladders were harvested for two different stress-relaxation experiments. Three bladders were used per each experiment (six total bladders harvested). Five samples of 1x3 cm strips cut from each bladder, totaling in 15 samples per experiment. Samples were mounted on the uniaxial machine via a clamp and submerged in Krebs solution 18 hours prior to testing.

Figure 14. A UB sample mounted on the uniaxial machine, submerged in Krebs solution.

The stress-relaxation test consisted of an instantaneous strain of 0.25 followed by a wait period of 30 minutes, a second strain increase of 0.25 followed by a 45 minutes wait period, and three incremental strain increases of 0.5 held for 45 minutes each (**Figure 15**).

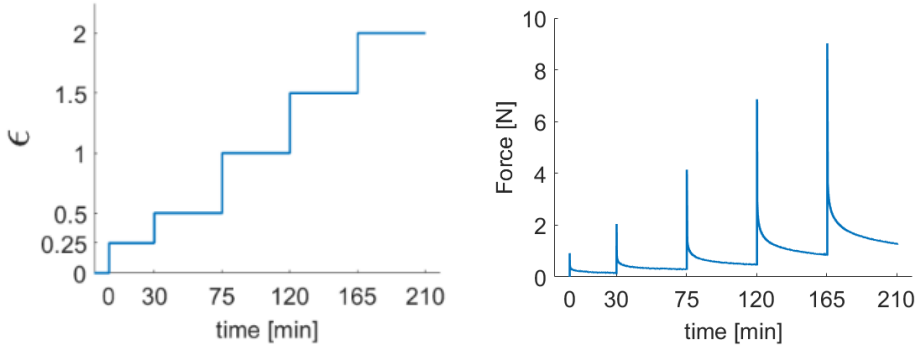

Figure 15. Five strains applied to the uniaxial machine (left) and the recorded stress relaxation behavior (right)

The first experiment was a test to identify differences between anatomical locations of the viscoelastic properties of the UB's wall. Samples were isolated from five locations: dorsal, ventral, lateral, lower body, and trigone (**Figure 16**). The Krebs solution used was 300 mOsm/L for all tests. The second experiment was a test to identify the effect of varying Krebs solution osmolarity (i.e., swelling) on the viscoelastic behavior of the tissue. For this experiment, five samples were all isolated from the lateral location (**Figure 16**). Four different osmolarity were tested, specifically 100, 300 (homeostatic), 600, and 900 mOsm/L; a fifth test was performed dry (without Krebs solution).

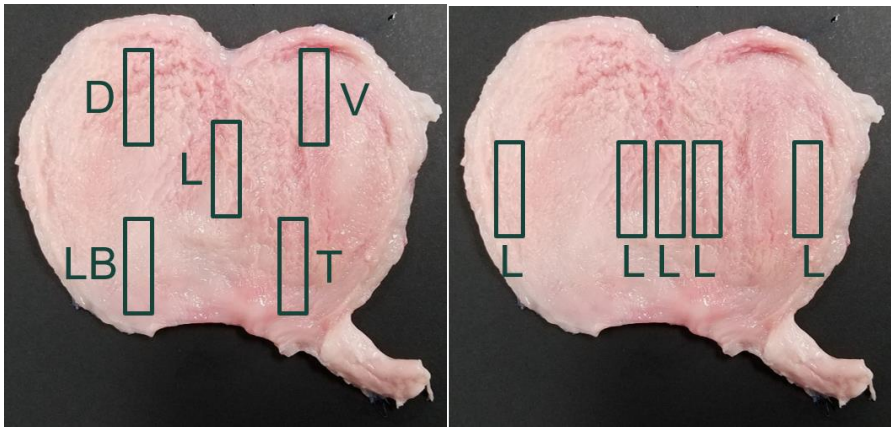

Figure 16. Samples cut for the location mechanical test, specifically dorsal (D), ventral (V), lateral (L), lower body (LB), and trigone (T) locations (left) and samples cut from the lateral location for the swelling test (right)

3.3. Previous Work

Prior to viscoelastic modelling of the data sets, analysis of the peak and relaxed stress was performed by Tyler Tuttle, who presented the following results at the 8th World Congress of Biomechanics in 2018 [Tuttle and Roccabianca, 2018]. Average peak stresses and relaxed stresses are plotted for location trials (**Figure 17**) and swelling trials (**Figure 18**). A two-way ANOVA was performed to compare significant differences among the trials. The p-values for the results are given for location (**Table 3**) and for swelling (**Table 4**).

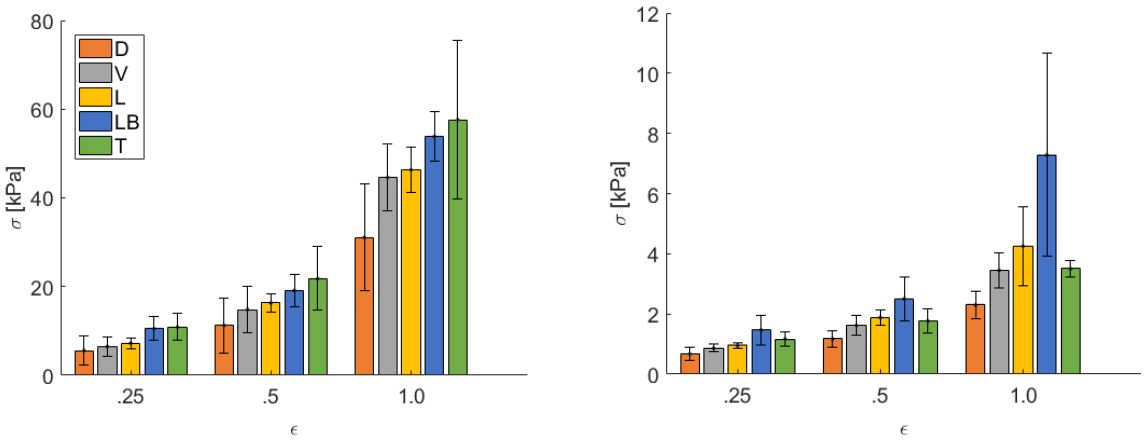

Figure 17. Average peak stresses for first three strains 0.25, 0.5, and 1.0 for peak stresses (left) and relaxed stresses (right) for location trials

V	L	LB	T	Location
0.35	0.225	0.01	0.002	D
	0.696	0.312	0.154	V
		0.458	0.266	L
			0.754	LB

V	L	LB	T	Location
0.743	0.406	0.001	0.616	D
	0.864	0.023	0.761	V
		0.107	0.906	L
			0.046	LB

Table 3. P-values comparing statistical significance between peak stresses (left) and relaxed stresses (right) based on anatomical location

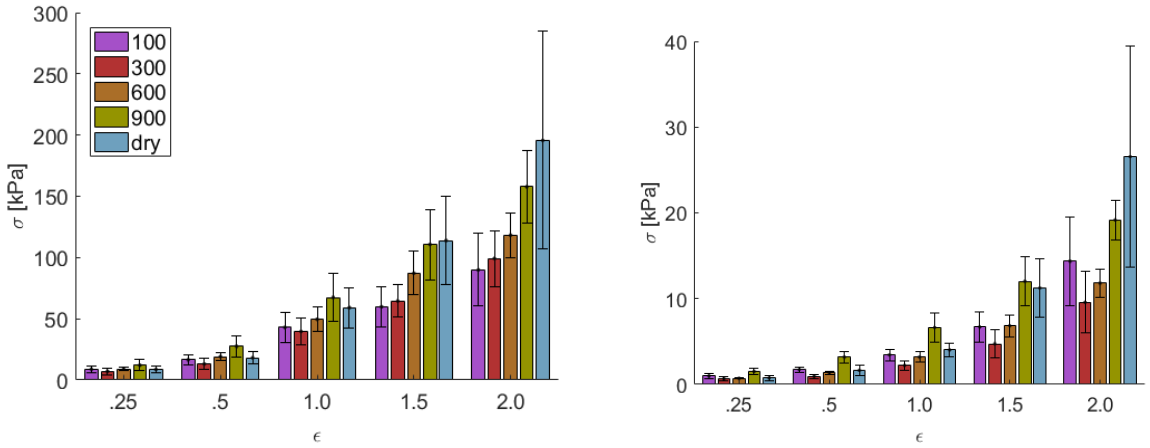

Figure 18. Average peak stresses for first three strains 0.25, 0.5, and 1.0 for peak stresses (left) and relaxed stresses (right) for swelling trials

300	600	900	dry	Osmolarity [mOsm/L]
0.907	0.532	0.011	0.004	100
	0.511	0.014	0.005	300
		0.245	0.115	600
			0.893	900

300	600	900	dry	Osmolarity [mOsm/L]
0.584	0.869	0.149	0.101	100
	0.794	0.008	0.004	300
		0.066	0.039	600
			0.809	900

Table 4. P-values comparing statistical significance between peak stresses (left) and relaxed stresses (right) based on bath osmolarity

There were statistically significant differences ($p<0.05$) between dorsal/lower body, 900 and 300 mOsm/L, and dry and 300 mOsm/L for both peak and relaxed stresses. In general, the trigone and lower body behaved differently than the dorsal and ventral regions. Samples tested dry and with 900 mOsm/L had higher stresses than other swelling trials. These results motivated us to fit parameters to the entire stress relaxation to see if viscoelastic behavior is different between anatomical regions and bath osmolarity.

3.4. Optimization Method

Model parameters were fit to the data by minimizing the root mean square error (RMSE) between theoretical and experimental stress relaxation curves through an iterative process shown in **Figure 19**. The minimization was performed using the MATLAB function "fminsearch". RMSE for Model (1) was based on the forces (**Eq. 36**). Models (2) – (4) calculated RMSE based on stress (**Eq. 37**).

$$RMSE = \sqrt{\sum \frac{(F_{Theory} - F_{Experiment})^2}{N}} \tag{36}$$

$$RMSE = \sqrt{\sum \frac{(\sigma_{Theory} - \sigma_{Experiment})^2}{N}} \tag{37}$$

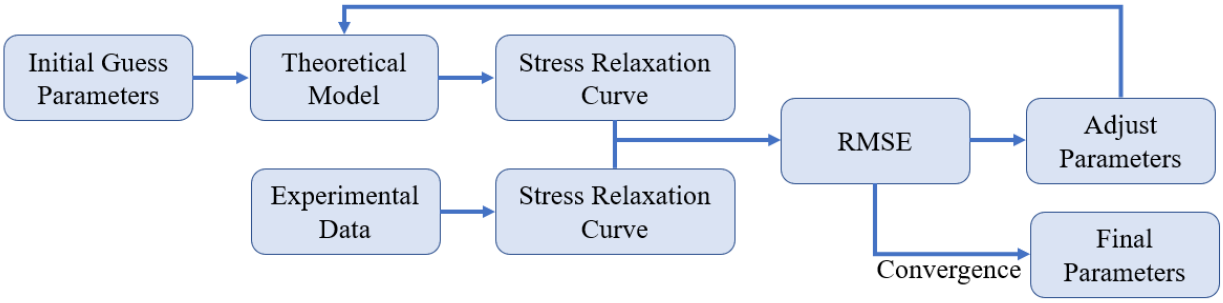

Figure 19. Diagram of the optimization procedure

3.5. Model 1: Quasilinear Viscoelasticity in FEBio, Single Stress-Relaxation

3.5.1. FEBio Model

For this method, FEBio, an open source software developed by Musculoskeletal Research Laboratories at University of Utah, was used to create a finite element model of our experiment. The reasoning for using FE for a 1D problem (which does not require 3D modelling) was so that this work can translate to 3D models of the whole bladder in future projects. The material chosen was Quasilinear Viscoelasticity with a neo-Hookean elastic component. The second Piola Kirchhoff stress for this material is defined as:

$$\boldsymbol{S}(t) = \int_{-\infty}^{t} G(t-s)\frac{d\boldsymbol{S}^e}{ds}ds, \tag{38}$$

where $\boldsymbol{S}^e$ is the elastic stress component and G(t) is the relaxation functions defined as:

$$G(t) = 1 + \sum_{i=1}^{n} \gamma_i \exp\left(-\frac{t}{\tau_i}\right). \tag{39}$$

Note that this is not the same as a *reduced* relaxation function which follows the condition $G(0) = 1$. The elastic copmonent $\boldsymbol{S}^e$ is related to the strain energy function by $\boldsymbol{S} = \frac{\partial W}{\partial \boldsymbol{E}}$. Lastly, the strain energy function W used here neo-Hookean, defined as:

$$W = \frac{\mu}{2}(I_1 - 3) - \mu \ln J + \frac{\lambda}{2}(\ln J)^2, \tag{40}$$

where the parameters are defined as $\lambda = \frac{vE}{(1+v)(1-2v)}$ (**Eq. 6**), $\mu = \frac{E}{2(1+v)}$ (**Eq. 7**), $J = \det(\boldsymbol{F})$, and $I_1 = \mathrm{tr}\,\boldsymbol{C}$. Our model used a relaxation function with n = 3, so the inputs to this model were $v, E, \gamma_1, \gamma_2, \gamma_3, \tau_1, \tau_2,$ and τ_3.

The recorded experimental data was assumed to be the force acting on the thinnest cross-section of tissue (**Figure 20**). The theoretical model forces at the cross section located on the Y-Z plane (surface B in **Figure 21** and **Figure 22**) were calculated from the outputs of Y-displacement, Z-displacement, and X-stress.

$$F_{Theory} = 4 * (z_0 - 2 * z_{max}) * (y_0 - 2 * y_{max}) * \sigma_{x,ave} \tag{41}$$

Force was used for the optimization of the material parameters so that data could be compared directly from experiments, without conversion to stress based on changing cross-sectional area.

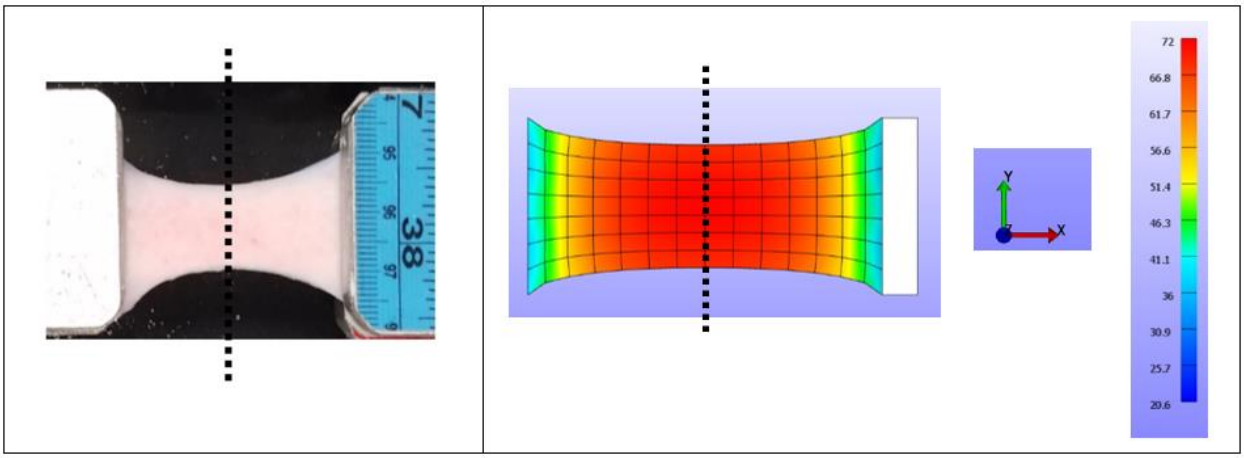

Figure 20. Porcine UB mounted on the uniaxial machine (left) and an early FE model of the experiment showing stress in the x-direction (right) and the cross section where the forces were calculated as a dotted line

Considering the symmetry of the problem, we included in the FE model created in FEBio 1/8th of the original 1x1x0.5 cm sample (**Figure 21**). A 7x7x7 elements mesh was used with bias in the x-direction to capture the stresses at the cross section of interest. The model assumes no slippage of the tissue in the clamps, as pictured above in **Figure 20**, represented by a rigid contact between the tissue model and the rigid body (representing the clamp). A displacement of the rigid body based on the first strain was then applied followed by 1800 seconds (30 minutes) of stress relaxation. Only the first strain was applied in FEBio. The parameters optimized for this approach were Young's Modulus E, and the relaxation strengths $\gamma_1, \gamma_2,$ and γ_3 associated with the relaxation times $\tau_1, \tau_2,$ and τ_3 from **Eq. 39**. The relaxation times were constants, the reasoning for which was discussed in **Section 2.5.3**.

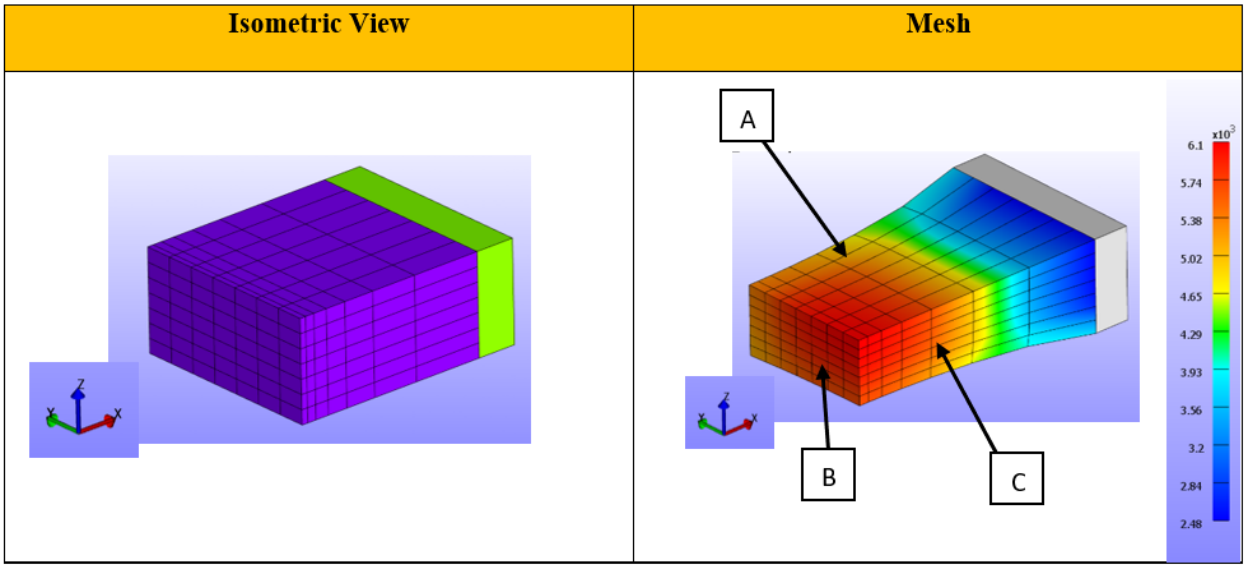

Figure 21. An isometric view of 1/8th the original tissues with a 7x7x7 mesh (left) and the stress of the model immediately after the first strain where the color bar is stress [Pa] and surfaces A, B, and C are cross sections shown in **Fig. 22** (right)

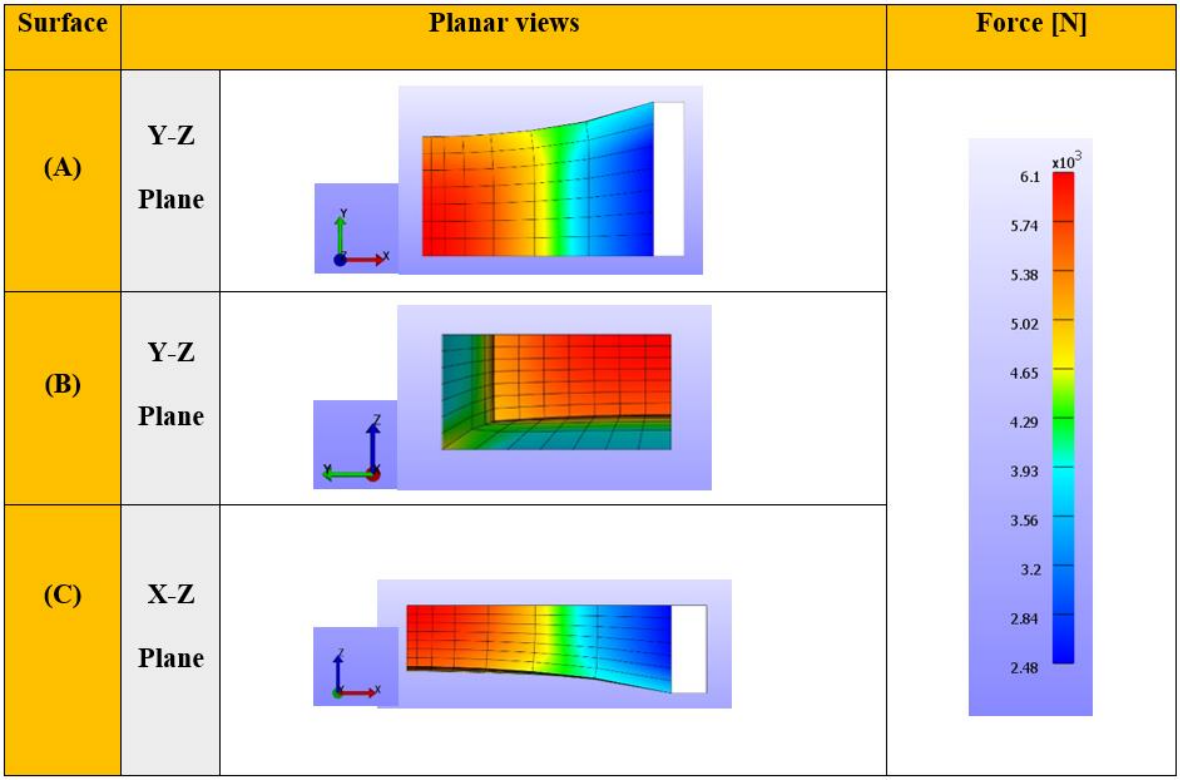

Figure 22. FEBio model during a relaxation phase showing 1/8th of the original tissue at different cross sections (labelled in **Fig. 21** above)

3.5.2. Methods: Initial Results

The first attempts to fit parameters to the FEBio model used the optimization procedure outlined in **Figure 19**. Unfortunately, this method allowed the optimization to end prematurely at local minima. We know this is a local minimum because manually fitting parameters was more precise. An example of this is seen in **Figure 23**. In this example, time steps assigned in FEBio were spaced 1 second apart for the first 100 seconds, and 10 seconds apart for the final 1700 seconds (for a total of 30 minutes).

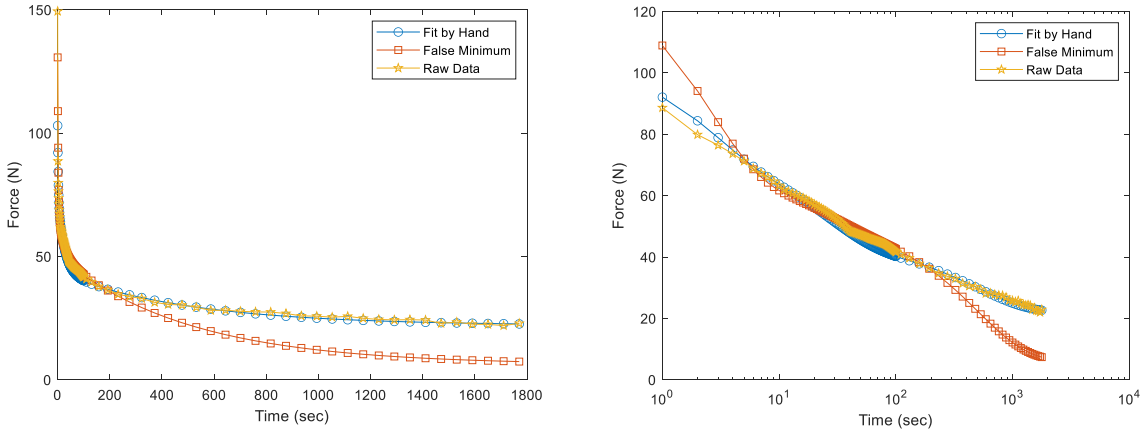

Figure 23. Optimization by procedure in **Fig. 23** (RMSE = 6.29) versus hand fitted results (RMSE = 4.35) and raw data on a normal time scale (left) and logarithmic time scale (right)

The reason for MATLAB finding a false minimum became clear after performing a parametric study. Stress is sensitive to Young's Modulus E for the entire curve. Young's Modulus E also decides the asymptote that stress relaxes to (elastic modulus times the strain) seen in **Figure 15**. Stress is sensitive to any given relaxation pair τ_i and γ_i only up until $t = 10^{\log(\tau_i+1)}$, one logarithmic decade following τ_i, as seen in **Figure 24**. This is the time after τ_i when the i^{th} relaxation pair are fully relaxed. The time $t = \tau_i$ marks the inflection point of the isolated relaxation pair on a logarithmic time scale.

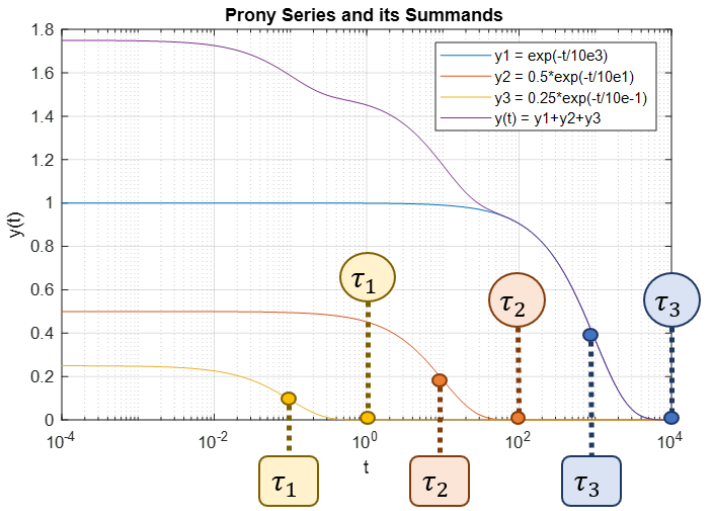

Figure 24. Relaxation times (pictured $\tau_1 = 10^{-1}s, \tau_2 = 10^1\ s,$ and $\tau_3 = 10^3 s$) are the location of the inflection point, on the logarithmic time scale, of the individual exponentials (boxes) and they decay to approximately zero within one logarithmic decade (bubbles)

MATLAB's "fminsearch" works by taking one parameter at a time, increasing and decreasing its value, assessing the new function value (RMSE in this case), and altering the parameter once more based on the gradient it found for that single parameter. It repeats this process for every parameter until the function value has converged, meaning it has reached a local minimum. This does not work well for functions with multiple minima, as in the relaxation function we are using. The reason for this is that it does not consider locational parameter sensitivity (seen in **Figure 13**), (2) inter-parameter sensitivity (discussed in **Section 2.5.3.**), and (3) the magnitude at which it must change parameters to escape a local minimum.

There may be many ways to approach this problem, such as a genetic algorithm (discussed in **Section 2.4.3.**) that is equipped to handle parameter relationships. Another approach would be a weighted error function that gives equal importance to different time sections. For the initial optimization results, equally spaced time steps give a heavier weight to Young's modulus and γ_3 than to say, γ_1 which decays quickly after $\tau_1 = 2.5\ s$. The last approach would be to force the optimization process by fitting parameters only to the sections they have the largest impact on. We chose this approach over a weighted error function due to shorter run times of the code.

3.5.3. Methods: Guided Optimization for Quasilinear Viscoelasticity

As discussed in the literature review, there may be infinite solutions to this model. Parameter optimization using "fminsearch" cannot fit parameters accurately on its own without either a weighted error or through sectioning. To solve this issue, we implemented a step-by-step optimization process that accounted parameter sensitivity to locations along the x-axis. RMSE is calculated for individual sections, most affected by certain parameters. To section the curve appropriately we used a geometric mean between time constants, which will be denoted as τ_{gm}. As seen in **Figure 25**, the geometric mean between two times τ_{n-1} and τ_n is a good cutoff point as long as they are one logarithmic decade apart ($\log(\tau_{n-1}) - \log(\tau_{n-1}) \geq 1$).

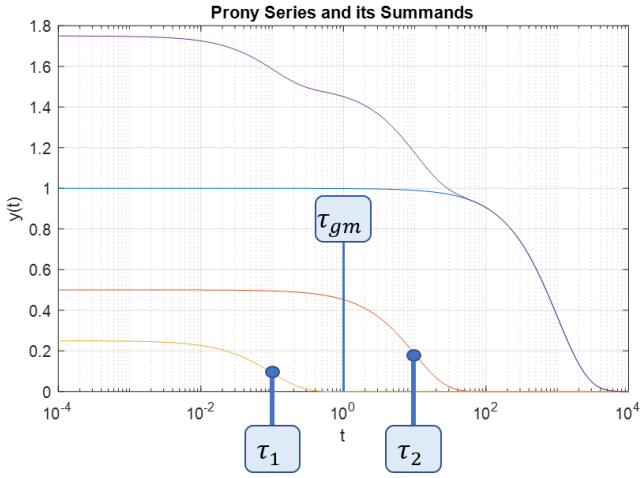

Figure 25. The geometric mean between two time constants τ_n and τ_{n-1} is the logarithmic hallway point where the decay from τ_{n-1} is complete if $\log(\tau_{n-1}) - \log(\tau_{n-1}) \geq 1$.

The steps of the optimization process were as follows:

1) Fit Young's Modulus to the relaxed stress only
2) Fit γ_n to section between the τ_{gm} and τ_n, where τ_{gm} is the geometric mean defined as:

$$\tau_{gm} = (\tau_n * \tau_{n-1})^{\frac{1}{2}}$$

3) Repeat step (2) until reaching $n = 1$, fit γ_1 from $t = 0$ to τ_1

Figure 26 shows which step uses which section for a Prony Series with n = 3. τ_n must be chosen at least one logarithmic decade apart for the geometric mean to work as intended.

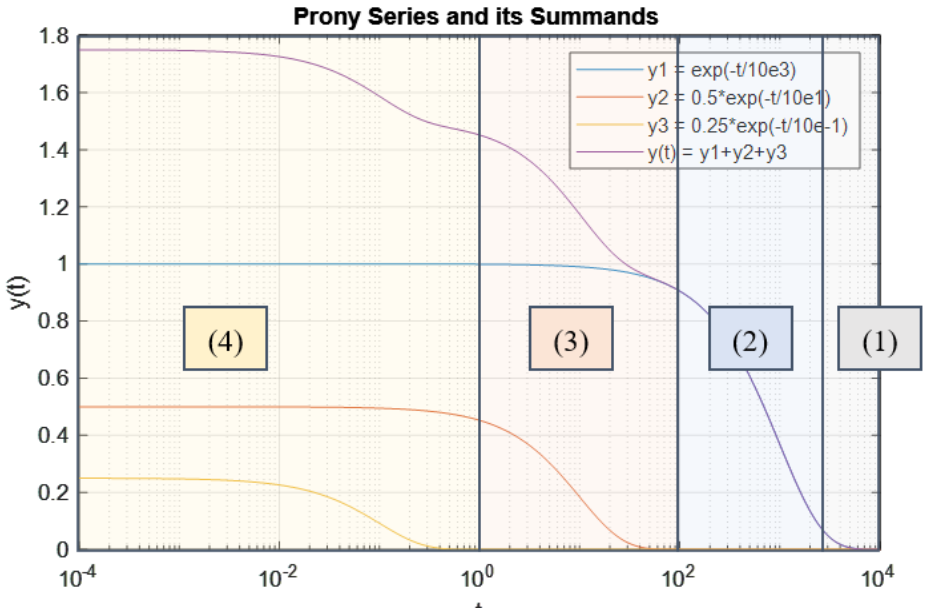

Figure 26. Sections numbered in order that they are used for fitting parameters where section (1) is used for step (1), section (2)-(3) are used for step (2) where $\tau_{gm} \leq t \leq \tau_n$, and section (4) is used for step (3)

These steps ensured that constants were fit only to portions of the curve that were sensitive to their changes. Time constants were chosen by manually fitting parameters. The time constants $\tau_1 = 2.5$ s, $\tau_2 = 25$ s, and $\tau_3 = 500$ s were then used for every sample.

3.5.4. Results

In the following table $\gamma_1, \gamma_2,$ and γ_3 belong to $\tau_1 = 2.5$ s, $\tau_2 = 25$ s, and $\tau_3 = 500$ s respectively, and E is Young's Modulus for the Neo-Hookean elastic component.

Experiment	Trial	γ_1	+/-	γ_2	+/-	γ_3	+/-	E (kPa)	+/-
LOCATION	D	2.80	1.24	2.01	0.61	1.52	0.42	6.20	1.70
	L	2.16	0.23	1.32	0.24	1.09	0.22	11.61	3.13
	LB	2.11	0.20	1.51	0.33	1.28	0.08	7.28	1.46
	T	2.93	0.56	2.43	0.24	1.40	0.25	6.24	0.85
	V	2.94	1.04	1.72	0.18	1.20	0.24	8.50	2.32
OSMOLARITY	100	2.04	0.65	1.10	0.50	1.10	0.20	13.14	5.29
	300	2.61	0.57	1.29	0.64	1.29	0.06	6.79	1.26
	600	2.52	0.12	1.56	0.23	1.56	0.21	7.74	1.55
	900	1.76	0.23	1.07	0.42	1.07	0.08	15.04	3.36
	dry	3.20	0.38	1.27	0.45	1.27	0.33	6.20	0.67

Table 5. Average fitted parameters by anatomical location (top) and bath osmolarity (bottom) for the linear viscoelastic FEBio model (model 1)

Experiment	Trial	RMSE
LOCATION	D	3.22
	L	3.92
	LB	2.85
	T	3.39
	V	3.90
OSMOLARITY	100	4.77
	300	3.20
	600	3.91
	900	5.07
	dry	2.84

Table 6. Average RMSE values for model (1)

The dorsal location showed a high standard deviation for γ_1 and many of the Young's modulus parameters had high standard deviations as well. The average parameters in **Table 5** were used to plot the stress relaxation and RRF by rerunning the model through FEBio. The following figures show the average curves first for the location experiments (RRF in **Figure 27**, stress-relaxation profile in **Figure 29**) and second for the swelling experiments (RRF in **Figure 28**, stress-relaxation profile in **Figure 30**).

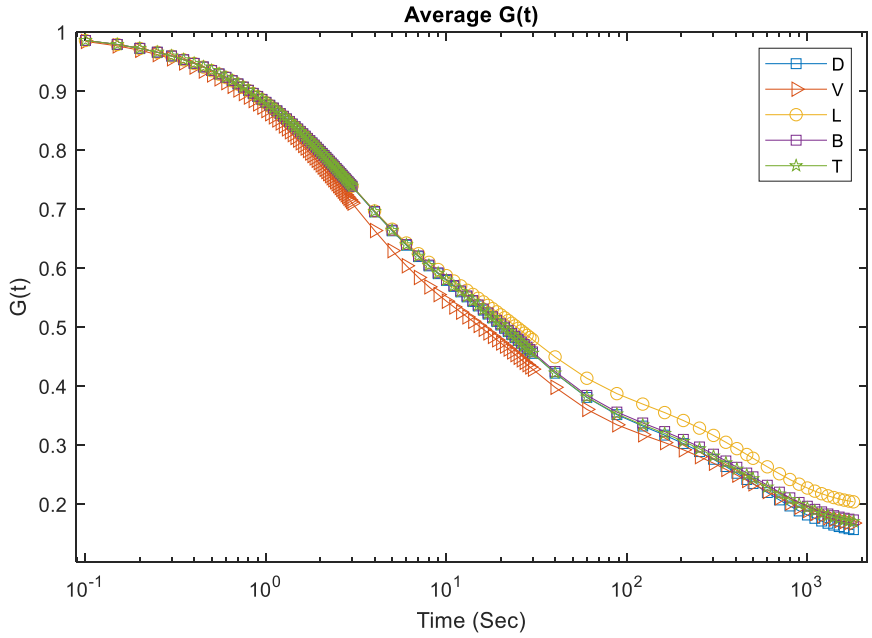

Figure 27. Average RRF (G(T)) plotted for each anatomical location dorsal (D), ventral (V), lateral (L), lower body (B), and trigone (T) for model (1)

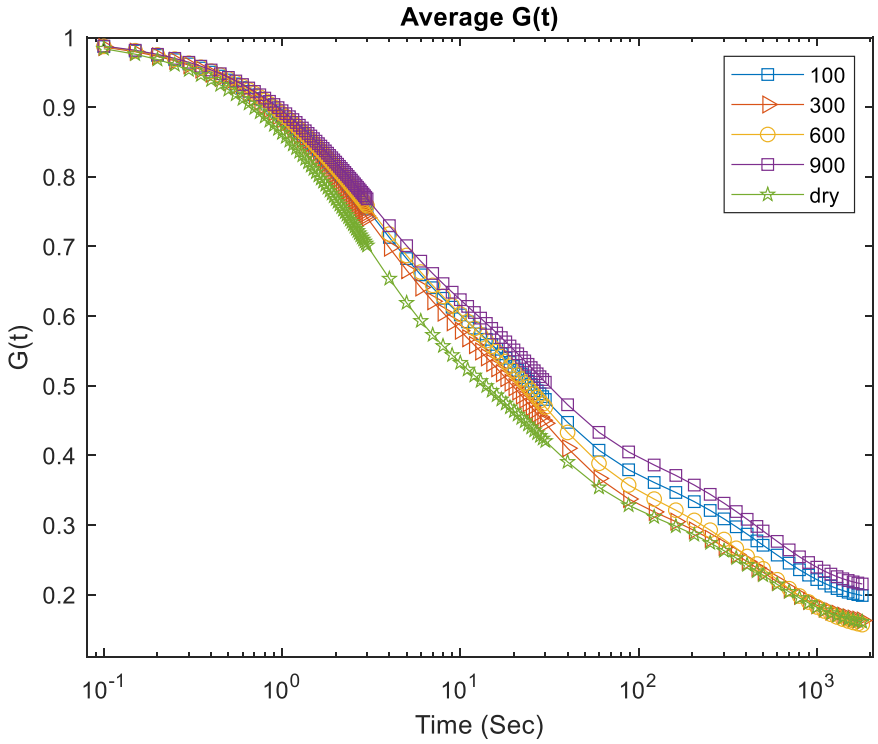

Figure 28. Average RRF plotted for each osmolarity trial 100, 300, 600, and 900 mOsm/L and dry for model (1)

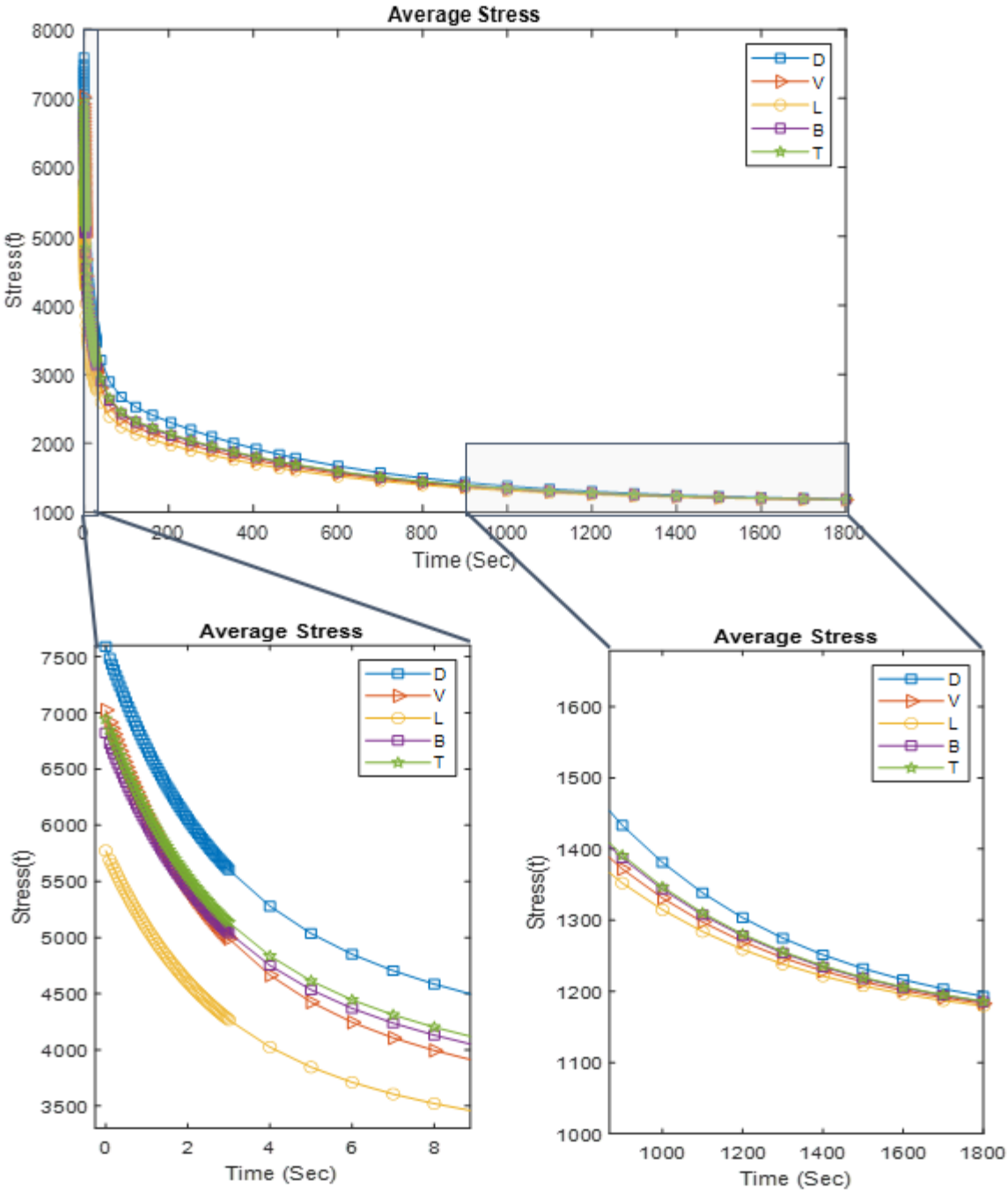

Figure 29. Average stress relaxation curves plotted for each anatomical location dorsal (D), ventral (V), lateral (L), lower body (B), and trigone (T) for model (1)

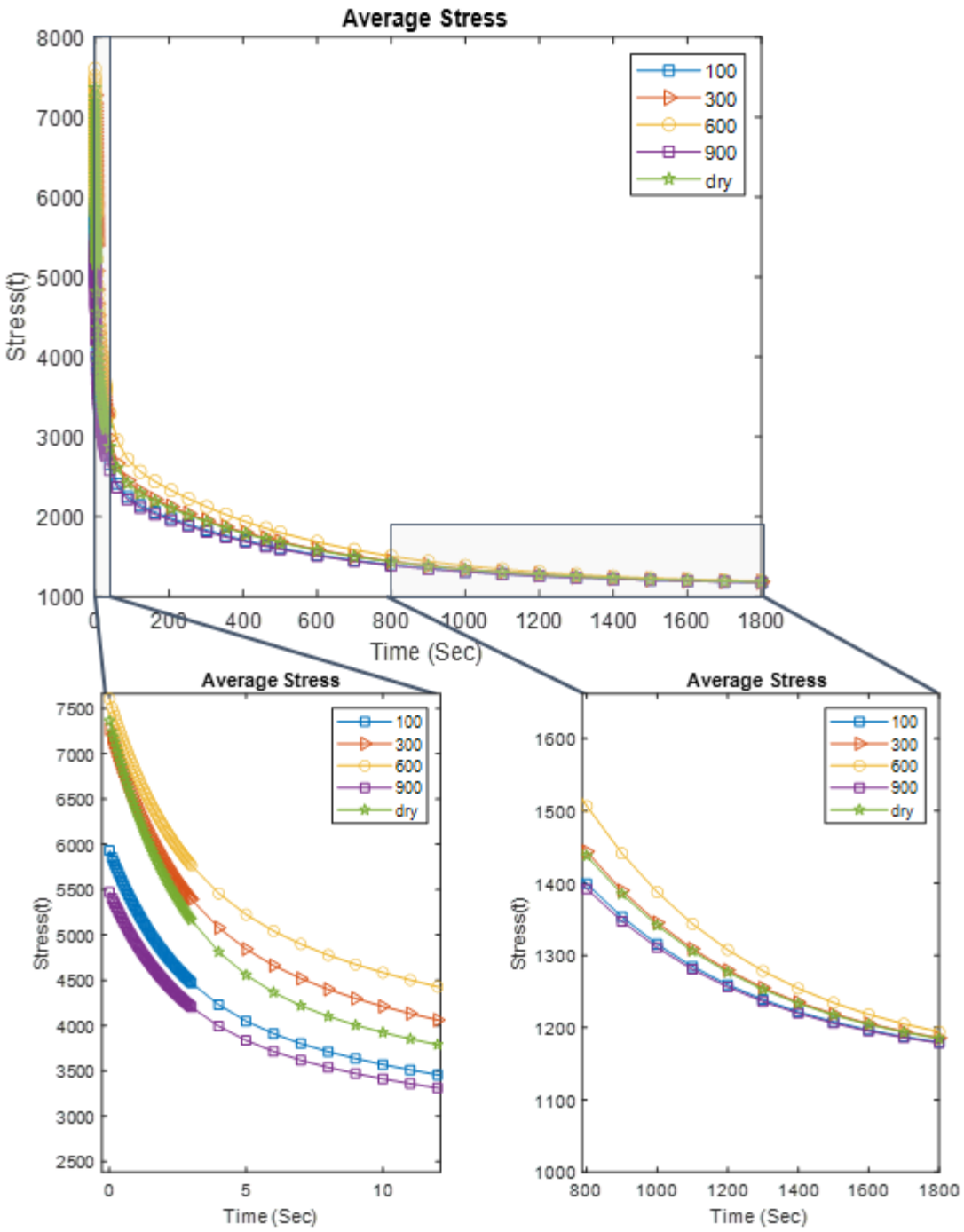

Figure 30. Average stress relaxation curves plotted for each osmolarity trial 100, 300, 600, and 900 mOsm/L and dry for model (1)

The RRF show different characteristics from the stress relaxation curves. For example, the lateral location had the lowest peak and relaxed stresses but higher values in the RRF. A higher RRF is generally related with less stress-relaxation capability and decreased compliance. The dorsal location had the highest peak and relaxed stresses but had an average RRF compared to all locations. Samples with 100 and 900 mOsm/L had lower stress relaxation (higher RRF values), while at the same time these samples showed the lowest peak and relaxed stresses.

3.5.5. Discussion

One source of error for calculating the elastic component is that the tests might have been ramped to the next strain before reaching a fully relaxed state. In the experimental results, the most significant differences in peak and relaxed stresses by location and osmolarity were observed in the later pulls (i.e., at higher strains). This leads us to conclude that the parameters fitted to the first strain only might not reveal statistically significant differences between samples because of the low value of deformation applied. User bias is also introduced by using fixed relaxation times that might alter results with unknown magnitude of significance. Lastly, noise from data collection is very high at the peak stresses and might skew γ_1 results (as seen in higher standard deviation in the dorsal location). To reduce the number of parameters, reduce user bias, and fit data to all curves, a different approach was taken without FEBio.

3.6. Model 2: Weichert Model with Logarithmic Exponential Distribution

3.6.1. Methods

The strain history must be accounted for when modelling the incremental step strains of our stress-relaxation results. Therefore, the following model was derived from the Weichert model combined with a continuous relaxation function in place of a series of Maxwell elements:

$$\sigma_1(t) = E_1 * \epsilon_1 + E_2 * \epsilon_1 * \int_0^{\infty} S(\tau) e^{-\frac{t-\tau_i}{\tau}} d\tau \tag{42}$$

$$\sigma_i(t) = \sigma_{i-1}(t) + E_1 * (\epsilon_i - \epsilon_{i-1}) + E_2 * (\epsilon_i - \epsilon_{i-1}) * \int_0^{\infty} S(\tau) e^{-(t-\tau_i)/\tau} d\tau \quad (43)$$

Where E_1 is the elastic modulus, E_2 is the elastic modulus of the viscoelastic component, ϵ_i is the current strain state, ϵ_{i-1} is the previous strain state, $\sigma_i(t)$ is stress as a function of time during the i^{th} stress-relaxation step, $\sigma_{i-1}(t)$ is the stress as a function of time from the previous strain, and $S(\tau)$ is a continuous distribution function. To minimize the number of parameters, a logarithmic exponential distribution function [Tahmasbi and Rezaei, 2008] that uses two parameters (β, p) was chosen to describe $S(\tau)$:

$$S(\tau) = \left(\frac{1}{-\ln p}\right) \frac{\beta(1-p)e^{-\beta\tau}}{1 - (1-p)e^{-\beta\tau}} \quad (44)$$

The parameters E_1, E_2, β, and p were fit to the entire strain history via **Eq. 43** and **Eq. 44**.

3.6.2. Results

Experiment	Trial	E_1 (kPa)	+/-	E_2 (kPa)	+/-	p	+/-	β	+/-
LOCATION	D	49.8	11.9	814.0	213.7	2.4E-05	1.1E-05	2.7E-03	8.6E-04
	L	27.4	5.9	664.3	19.9	4.0E-05	1.6E-05	3.7E-03	7.1E-04
	LB	36.6	6.0	874.5	135.0	2.6E-05	8.3E-06	2.5E-03	5.1E-04
	T	45.4	32.3	1121.3	132.8	5.3E-06	4.6E-06	1.2E-03	9.8E-04
	V	49.6	21.3	781.4	234.1	4.8E-05	2.8E-05	5.0E-03	2.3E-03
OSMOLARITY	100	28.0	8.7	650.2	101.3	1.8E-05	8.7E-06	2.5E-03	4.7E-04
	300	55.1	14.8	911.4	229.1	1.7E-05	7.3E-06	2.8E-03	7.4E-04
	600	37.9	12.8	609.7	179.9	1.6E-05	1.4E-05	3.0E-03	1.1E-03
	900	45.5	7.2	589.4	101.6	7.2E-05	4.1E-05	4.4E-03	1.3E-03
	dry	51.3	15.1	943.6	304.1	2.8E-05	7.0E-06	2.9E-03	8.5E-04

Table 7. Average fitted parameters fitted to **Eq. 43** and **Eq. 44** by anatomical location (top) and swelling (bottom) for the logarithmic exponential CRS (model 2)

Experiment	Trial	RMSE
LOCATION	D	17.21
	L	15.11
	LB	17.27
	T	24.36
	V	29.93
OSMOLARITY	100	11.60
	300	22.90
	600	16.06
	900	28.29
	dry	20.53

Table 8. Average RMSE values for model (2)

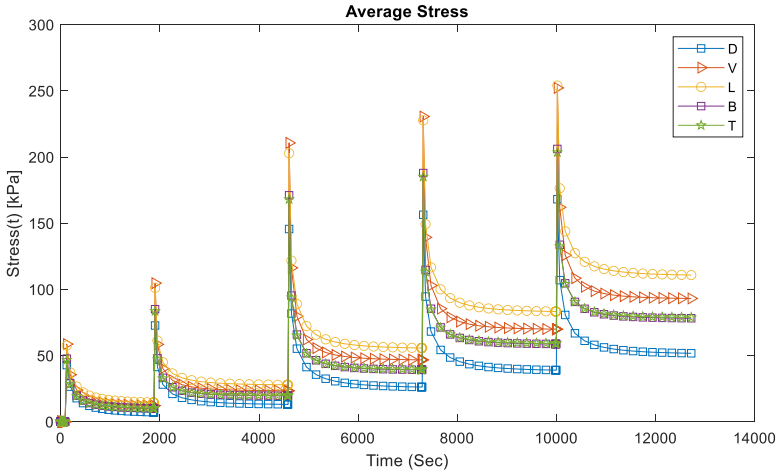

Figure 31. The incremental stress-relaxation curves for location trials using parameters from **Table 5** for model (2)

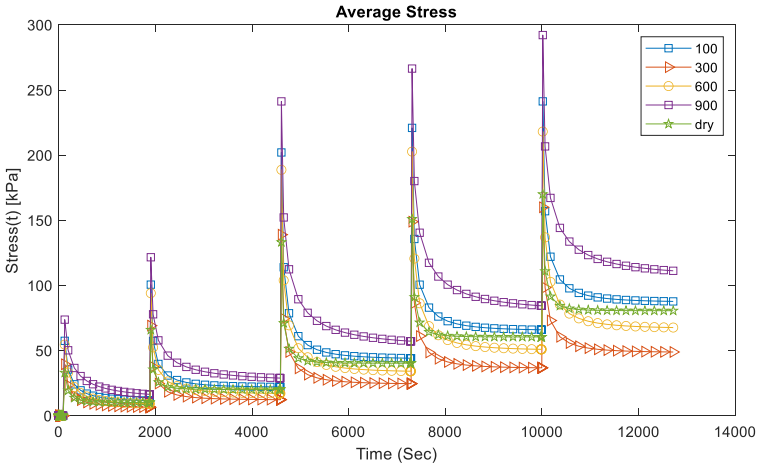

Figure 32. The incremental stress-relaxation curves for swelling trials using parameters from **Table 5** for model (2)

The trends shown by the average parameters reflect what observed in the experimental results for osmolarity trials but not for location trials. The peak and relaxed stresses were highest for 900 and 100 mOsm/L and lowest for 300 and 600 mOsm/L which confirms what observed in the experimental results. The lower body and trigone regions, however, had peak and relaxed stresses included within the range defined by the other locations, while they showed to have the highest values in the experimental results. Additionally, the differences between parameters are not statistically significant. A two-way ANOVA was performed to analyze differences between all parameters, and none showed significance. This is no surprise, considering that some of the standard deviations for the parameter *p* are rather large (i.e., lower body, 100 mOsm/L, and 900 mOsm/L). Additionally, the RMSE values were rather high as can be seen in **Table 8**.

3.6.3. Discussion

This model was found to be incapable of accurately fitting the data based on the high RMSE values and conflicting results for location trials. One limitation of this model is that it is not capable of capturing nonlinear elastic behavior of the elastic portion of the tissue. The theoretical curves increase in stress proportional to the strain (in the relaxed state) while the experimental stress seems to behave in a non-linear way. While some of the data were described rather accurately by this model, there were other datasets where the description was less accurate (**Figure 33**).

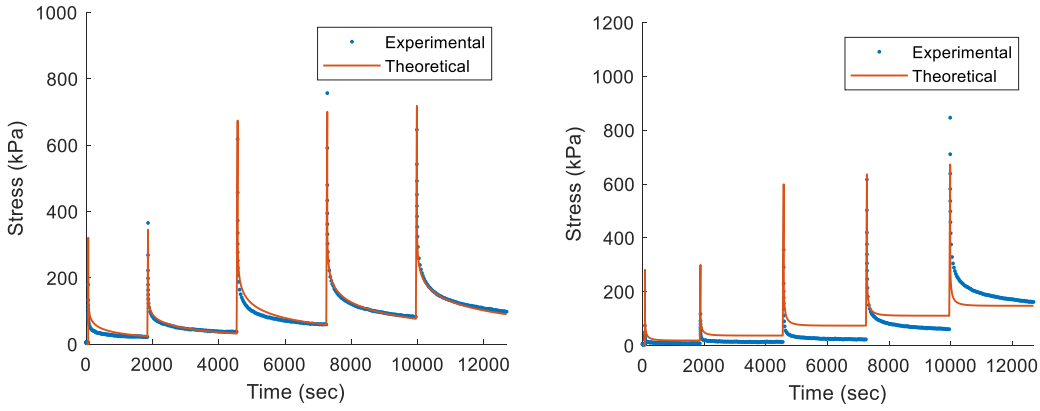

Figure 33. Experimental versus theoretical data for a good fit (bladder #2 900 mOsm/L) (left) and a bad fit (bladder #2 dry) (right) using model (2)

Other spectrums, such as the discrete spectrum for the Weichert model and gaussian CRS used by Nagatomi et al. (2008), were combined with **Eq. 43** but had the same consequences as the ones seen in **Figure 33**. Therefore, the Weichert model was abandoned for the remaining models while CRS continued to be tested.

3.7. Model 3: Reduced Relaxation Function with Log Normal Distribution ($n = 1$)

3.7.1. Methods

There are two possible approaches to describe incremental strains in a stress-relaxation test on nonlinear viscoelastic materials employing an RRF, although this has been rarely done in literature (see **Section 2.5.2.**). One approach consists of using QLV with but including a non-linear, hyperelastic component to describe the elastic portion of the response. The second approach is to model viscoelasticity by decoupling it from the nonlinear hyperelastic behavior. We will only use the second approach for the remaining models and discuss how to implement the first approach in the section on future work. We normalize each stress relaxation curve (five per data set) and fit a CRS to all five simultaneously. Each stress relaxation curve was normalized by the following equation (from Sarver et al., 2003):

$$\tilde{G}(t) = \frac{\sigma^i(t) - \sigma_f^i}{\sigma_p^i - \sigma_f^i} \ , \tag{45}$$

where $\sigma^i(t)$ is the current stress-relaxation, σ_f^i is the final (relaxed) stress for the current curve, and σ_p^i is the peak stress for the current curve seen in **Figure 34**.

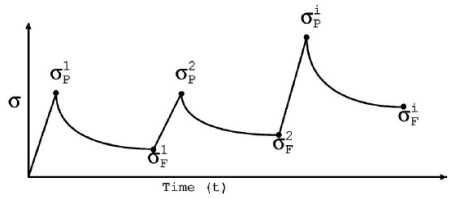

Figure 34. Peak and relaxed stresses for each stress relaxation curve are used to normalize the curve by **Eq. 45** [Sarver et al., 2003]

The normalization technique allows us to study the relaxation behavior without modelling the hyperelastic component. **Figure 35** shows how data normalized for all strains have similar relaxation behavior.

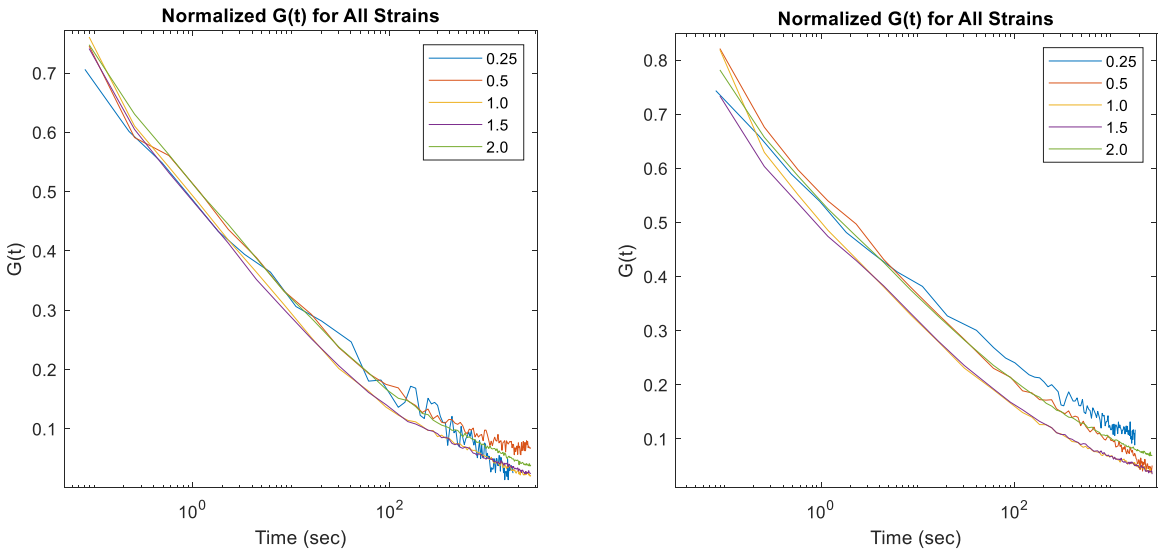

Figure 35. Normalized $\tilde{G}(t)$ for all strains in the same experiment bladder #6 dorsal (left) and bladder #3, 100 mOsm/L (right) show no trends in increasing final stress that are seen in the nonnormalized data

We employ here the dual gaussian relaxation spectrum with $n = 1$ [Nagatomi et al., 2008] and optimize the parameters $\mu, \sigma,$ and a:

$$S(\tau) = \sum_{m=1}^{n} a_m \frac{\exp\left\{-\frac{1}{2}\left[\frac{(log_{10}\tau - log_{10}\mu_m)}{log_{10}\sigma_m}\right]^2\right\}}{log_{10}\sigma_m\sqrt{2\pi}}, \tag{31}$$

$$G(t) = \frac{1 + \int_0^\infty S(\tau)e^{-t/\tau}d\tau}{1 + \int_0^\infty S(\tau)d\tau}. \tag{33}$$

3.7.2. Results

Experiment	Trial	μ	+/-	σ	+/-	a	+/-
LOCATION	D	6.4E-08	9.4E-08	73.44	15.17	4.4E+18	4.4E+18
	L	2.2E-09	2.7E-09	102.2	15.33	7.7E+18	8.5E+18
	LB	6.0E-10	4.3E-10	111.9	8.16	5.0E+18	5.5E+18
	T	1.7E-08	2.4E-08	93.60	27.03	7.9E+18	1.3E+19
	V	1.1E-08	1.1E-08	84.39	8.62	4.3E+18	4.4E+18
OSMOLARITY	100	1.6E-08	2.1E-08	85.79	13.92	8.4E+17	7.3E+17
	300	1.6E-07	7.5E-08	58.73	4.09	1.0E+18	9.6E+17
	600	1.3E-07	8.8E-08	61.74	4.90	3.6E+18	1.7E+18
	900	1.1E-09	9.6E-10	115.0	29.11	4.3E+19	2.6E+19
	dry	6.5E-08	9.4E-08	79.57	27.45	7.8E+17	1.3E+18

Table 9. Parameters for **Eq. 31** with n=1 fit to data for location trials (top) and swelling trials (bottom) for model (3)

Experiment	Trial	RMSE
LOCATION	D	0.11
	L	0.13
	LB	0.14
	T	0.16
	V	0.13
OSMOLARITY	100	0.15
	300	0.12
	600	0.10
	900	0.14
	dry	0.12

Table 10. Average RMSE values for model (3)

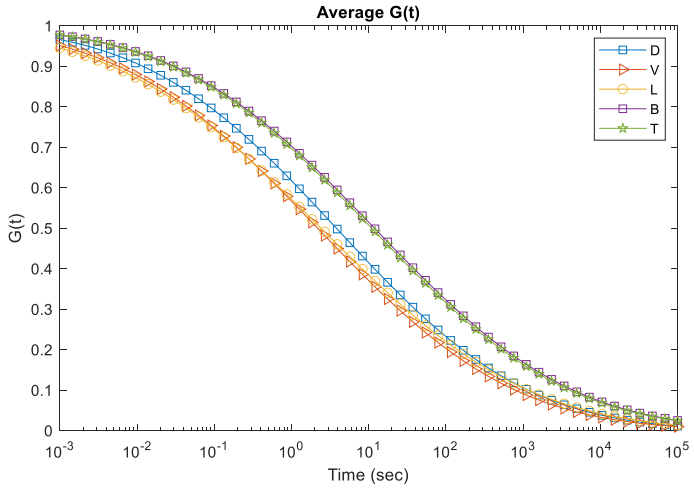

Figure 36. Average relaxation behavior (RRF) by location based on parameters from **Table 7** for model (3)

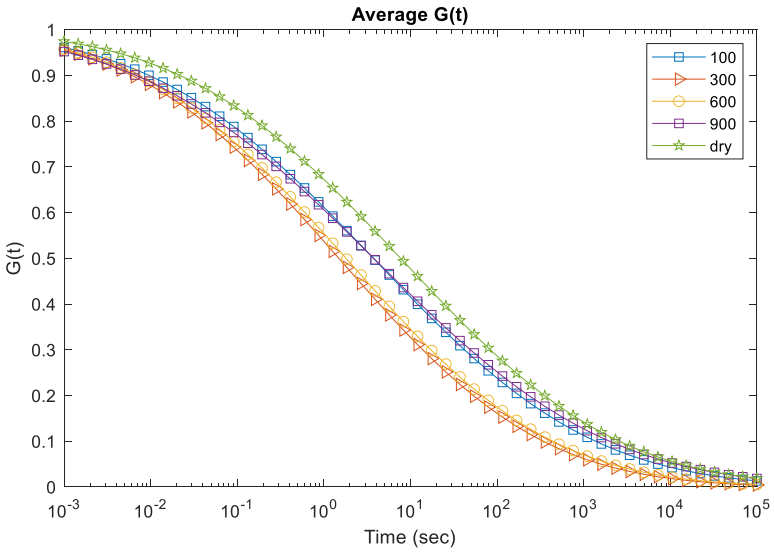

Figure 37. Average relaxation behavior (RRF) by bath osmolarity based on parameters from **Table 9** for model (3)

3.7.3. Discussion

The logarithmic exponential distribution from Model (2) was tested but had an asymptote at $G(t) = 0.5$ and could not be fit to the RRF. The CRS using a spectrum defined by **Eq. 31** with $n = 1$ matched predictions of behavior by location and osmolarity in terms of the overall RRF (**Fig. 36** and **Fig. 37**). Lower body and trigone regions had the lowest compliance among the location trials. The dry samples had the lowest compliance, 100 and 900 mOsm/L samples were the next lowest compliant, and 300 and 600 mOsm/L samples had the highest compliance. These results seem to agree with what observed experimentally, however the parameters themselves are too large to be analyzed by statistical software. Amplitude a is on the magnitude of 10^{18}. The values seem too large considering that the values reported in literature for a were on the magnitude of 10^{-1} [Nagatomi et al., 2008], so we suspect that this spectrum is not appropriate but that the normalization process improved results.

3.8. Model 4: Reduced Relaxation Function with Log Normal Distribution (n = 2)

3.8.1. Methods

A second trial of the dual gaussian spectrum (**Eq. 31)** used $n = 2$ and was able to fit results with smaller RMSE values on average than $n = 1$. Unfortunately, the double peaked spectrum is an ill-posed problem like the Prony Series, where there is no unique solution. Any change to the mean $log_{10}\mu_m$, requires an adjustment of its dependent parameters α_m and $log_{10}\sigma_m$. Additionally, the fitting process involves integration of the initial-guess spectrum, making it an inverse problem very sensitive to noise in the data.

An attempt to "guide" the optimization process is outlined in **Figure 38**. While we are aware of the "ill-posedness" of the problem, once the initial guess for each parameter is set, the solution is, if not unique, quite repeatable using this procedure. This assumption is supported by the empiric observation that reruns with the same initial guess resulted in the exact same results. For this reason, we worked on identifying educated guesses for each parameter's starting value. Initial values for the parameters were taken from Nagatomi et al. (2008) and are given below in **Table 11**.

μ_1	σ_1	a_1
7.192	9.616	0.281
μ_2	σ_2	a_2
2413	3.823	0.306

Table 11. Initial guess parameters from Nagatomi et al. (2008)

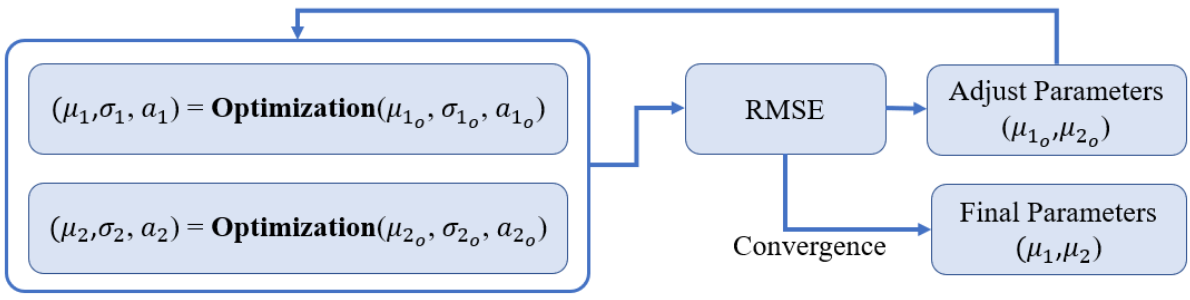

Figure 38. Guided optimization for Log-Normal Distribution (n = 2) where "Optimization" refers to the procedure outlined in **Fig. 19**

3.8.2. Results

	Experiment	Trial	μ_1	+/-	σ_1	+/-	a_1	+/-
m = 1 Parameters	LOCATION	D	2.8E-06	3.4E-06	44	14	4.5E+10	7.8E+10
		L	2.8E-06	1.6E-06	37	2.3	1.0E+06	1.5E+04
		LB	3.9E-06	3.4E-06	42	16	9.0E+07	1.6E+08
		T	3.8E-05	6.2E-05	34	10	7.7E+05	7.3E+05
		V	1.1E-05	7.3E-06	31	5.5	4.6E+05	1.7E+05
	OSMOLARITY	100	4.3E-06	6.2E-06	48	22	3.4E+12	5.9E+12
		300	1.9E-05	1.7E-05	33	11	1.7E+07	2.9E+07
		600	7.2E-03	1.2E-02	39	33	3.1E+10	5.4E+10
		900	6.4E-06	1.1E-05	63	43	4.5E+13	7.9E+13
		dry	8.0E-06	9.3E-06	42	20	1.0E+08	1.7E+08
	Experiment	**Trial**	μ_2	+/-	σ_2	+/-	a_2	+/-
m = 2 Parameters	LOCATION	D	1619	2399	2.6	2.2	0.36	0.09
		L	299.2	32.34	3.8	0.0	0.31	0.00
		LB	1227	1644	2.9	1.6	0.54	0.41
		T	326.2	32.24	3.8	0.0	0.30	0.00
		V	276.2	65.24	3.8	0.0	0.31	0.00
	OSMOLARITY	100	2023	2847	2.6	2.2	0.35	0.07
		300	685.8	786.6	2.9	1.6	0.66	0.62
		600	907.6	1405	2.6	2.3	0.34	0.09
		900	950.6	1371	2.6	2.3	0.37	0.14
		dry	1055	783.7	2.9	1.6	0.63	0.57

Table 12. Parameters for **Eq. 31** with n=2 fit to data for location trials (top) and bath osmolarity trials (bottom) for model (4)

Experiment	Trial	RMSE
LOCATION	D	0.15
	L	0.12
	LB	0.10
	T	0.13
	V	0.12
OSMOLARITY	100	0.11
	300	0.12
	600	0.14
	900	0.16
	dry	0.12

Table 13. Average RMSE values for model (4)

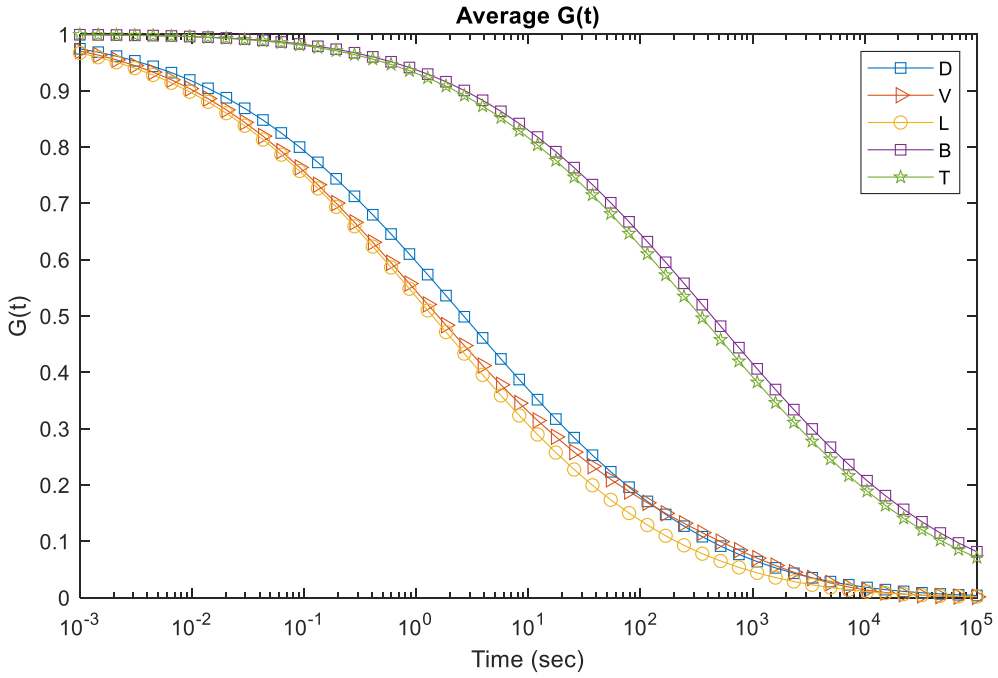

Figure 39. Average RRF based on parameters from **Table 12** for location trials for model (4)

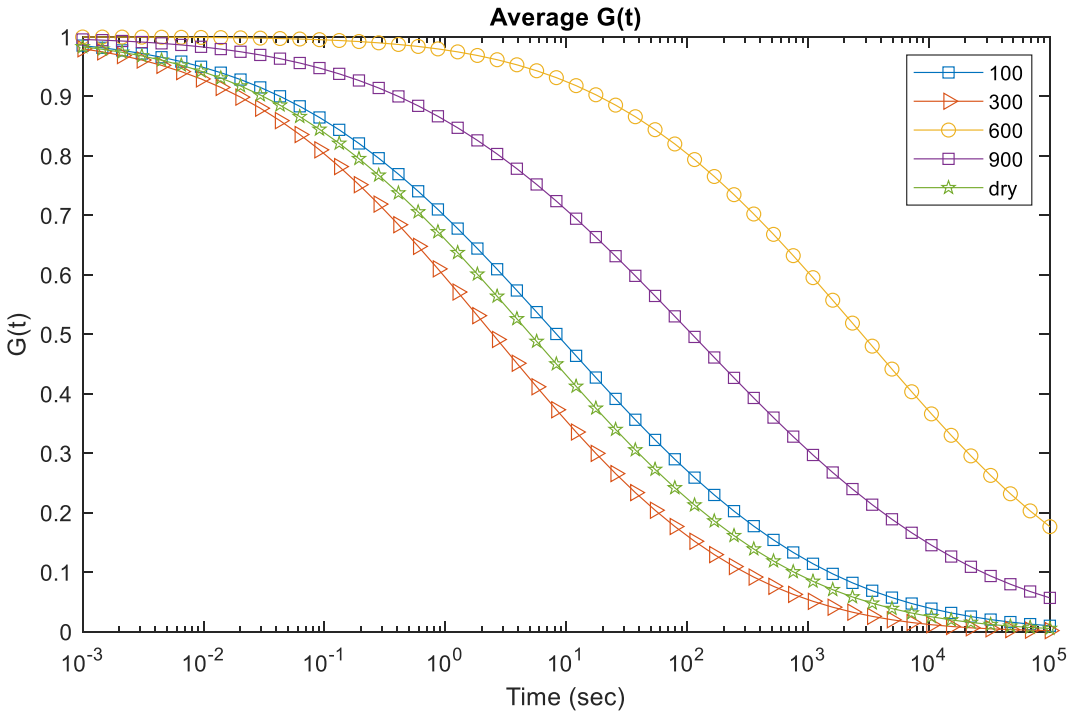

Figure 40. Average RRF based on parameters from **Table 12** for swelling trials for model (4)

3.8.3. Discussion

Results based on location strongly indicated lowered relaxation capability for lower body and trigone regions and 600 mOsm/L bath osmolarity. The results for bath osmolarity conflict with the results from the spectrum using $n = 1$. Although the location trials have plots that look like the expected behavior, we believe results are not representative because some of the standard deviations are rather large compared to the means.

3.9. Overall Conclusions

There were observable trends in the relaxation behavior of different locations. The trigone and lower body regions had lower stress relaxation (took longer to relax to the same stress) and higher final stresses. These trends are what we expect to see based on results from Korossis et al. for location. Similarly, swelling samples of the 900 mOsm/L, 100 mOsm/L, and dry tests had lowered stress relaxation and higher final stresses. While the trends are promising, the parameters that produce the average stress-relaxation curves failed p-tests.

3.9.1. Sources of Error

One source of error for all trials is that strains were re-applied before the sample reached a fully relaxed state, only observable on the logarithmic scale. This can skew the resulting parameters of the elastic portion of each model. A source of error for method (1) would be that choosing the time constants through a manual fitting could influence the results for $\gamma_1, \gamma_2, \text{and } \gamma_3$ and potentially Young's Modulus as can be seen in **Figure 13**. To eliminate error from time constant selection, the interconversion algorithms mentioned in the literature review would provide the best time constants without user bias because the discrete spectra are based on peaks in the continuous spectra (**Figure 12**). Method (4) is insufficient to fit the parameters when the spectrum is bimodal ($n = 2$). The authors who used this model on the UB mention the use of a genetic algorithm to solve this [Nagatomi et al., 2004]. A genetic algorithm might be more effective in fitting parameters for methods (1) and (4) because these the solutions are non-unique.

We speculate that an appropriate constitutive model might show statistically significant differences of viscoelastic parameters based on location and swelling.

3.9.2. Future Work and Works in Progress

There are other time spectrums that were not tested for methods (3) and (4) that might better fit our data such as the straight value spectrum (**Eq. 46**) which, when combined with equation **Eq. 32**, gives a generalized reduced relaxed function in the form of **Eq. 47**.

$$S(\tau) = \begin{cases} \frac{c}{\tau}, & \tau_1 \le \tau \le \tau_2 \\ 0, & otherwise \end{cases} \tag{46}$$

$$G(t) = \frac{1+c\left[E\left(\frac{\tau}{\tau_1}\right) - E\left(\frac{\tau}{\tau_2}\right)\right]}{1+c\ln\left(\frac{\tau_1}{\tau_2}\right)}, \quad E(z) = \int_0^\infty \frac{e^{-t}}{t}\,dt\,. \tag{47}$$

A second approach to account for the nonlinear viscoelastic behavior would be to use the FEBio model from method (1) and replace the linear elastic component with a nonlinear component. Manually fitted trials using EFD Neo-Hookean Elasticity were run on this model and show that it can fit relaxed stresses better than linear viscoelasticity. The downside is that the optimization process still arrives at false minima unsupervised (see **Figure 41**). This model will require the same guided optimization method used for Model (1).

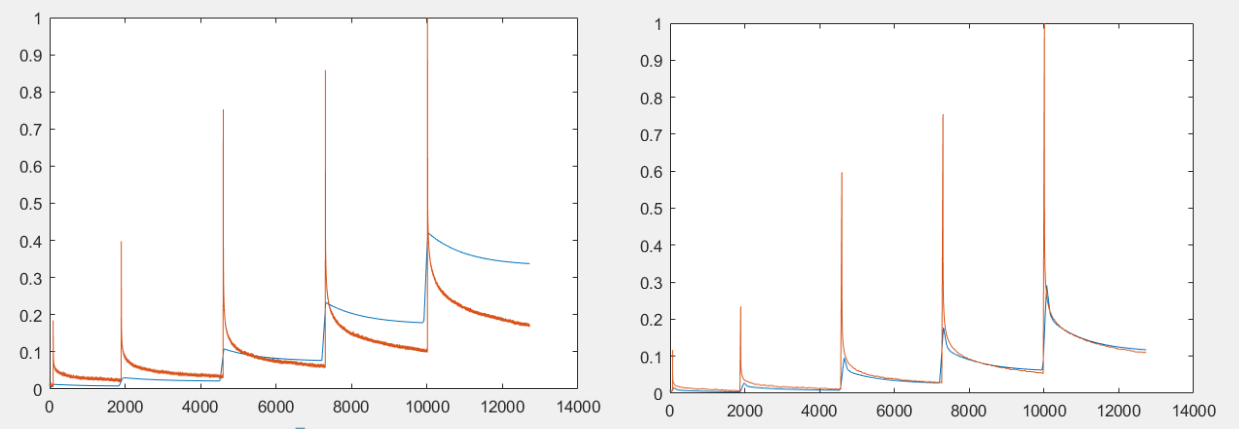

Figure 41. Viscoelastic solid with EFD neo-Hookean elastic component optimized in MATLAB (left) and manually fitted (right)

The swelling trials can also be improved with multi-phasic modelling. The FEBio model was re-designed as a triphasic material with a solid mixture of Donnan Equilibrium and neo-Hookean elastic component. A fixed charge density of the solid matrix was ramped from zero to 100 $[C \cdot \mathrm{m}^{-3}]$ during the first analysis step (**Fig. 42**. step A). The next step ramped the initial bath concentration of 300 mOsm/L from up to 900 mOsm/L for one run and down to 100 mOsm/L for a second run (**Fig. 42**. step B). Both runs were then strained to 0.25 (**Fig. 42**. step C). The last step is where stress relaxation is observed from fluid moving in or out of the porous solid (**Fig. 42**. step C). This proof-of-concept model showed that the different bath concentration led to different peak stresses, like our experimental results (**Figure 43**).

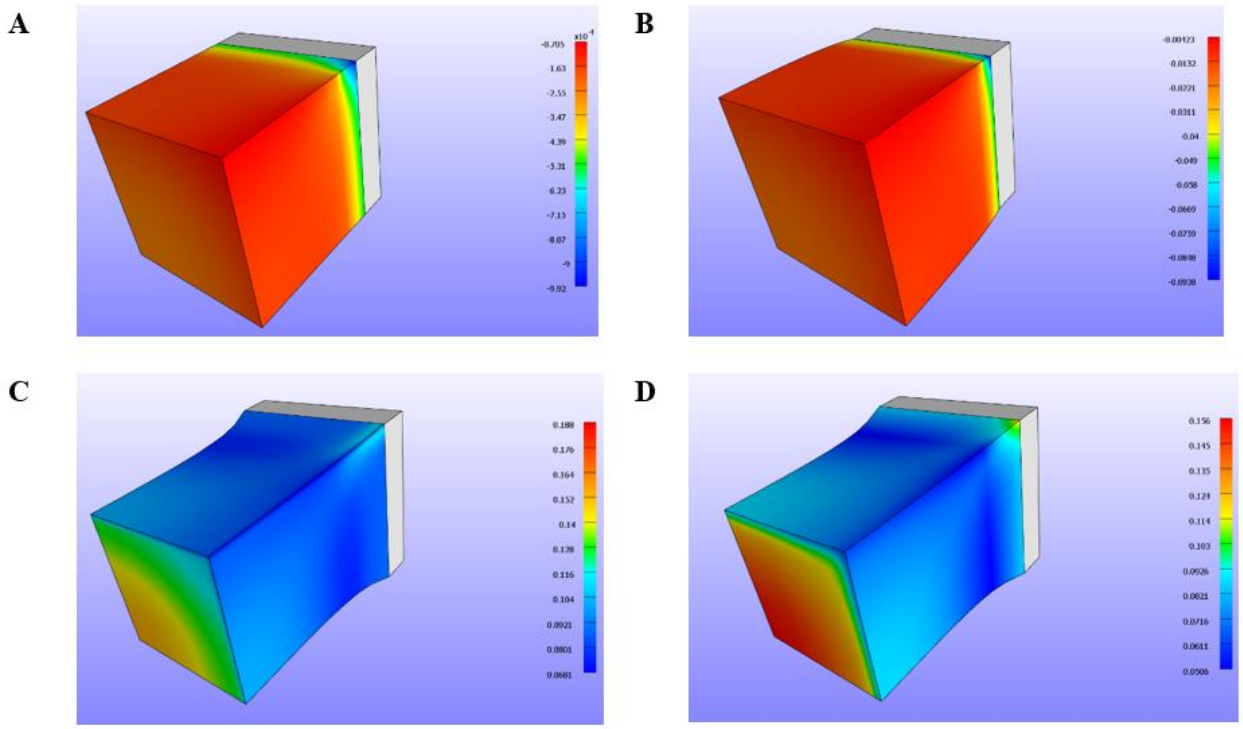

Figure 42. FEBio triphasic model showing stress in the x-direction in different stages (A) loading the fixed charge density of the Donnan Equilibrium neo-Hookean solid (B) loading the bath osmolarity (C) applying a strain to the specimen (D) the relaxation phase

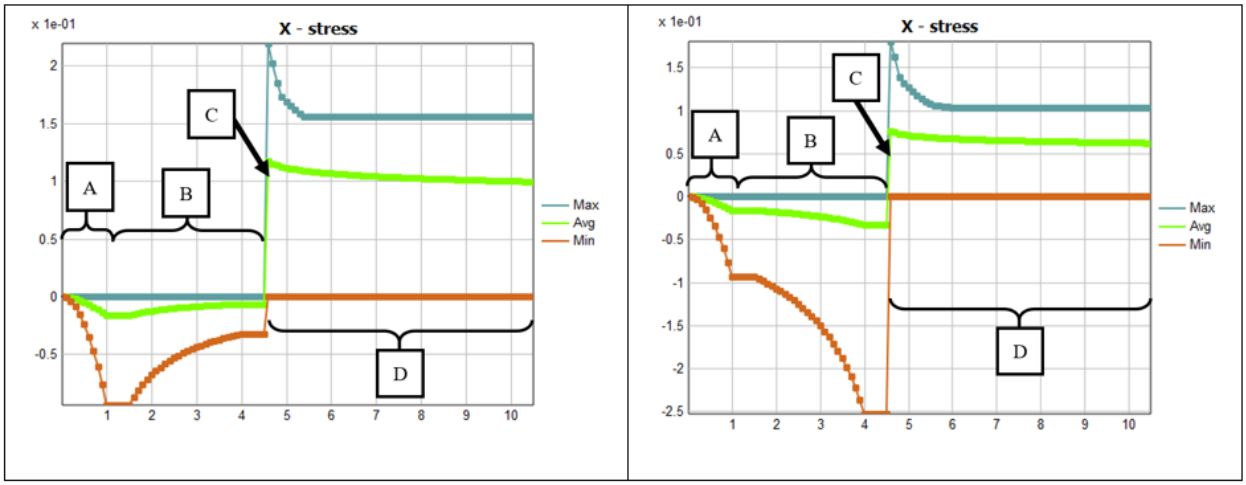

Figure 43. The x-stress through the different stages of analysis of triphasic solid showing higher peak stress for ramping bath osmolarity from 300 to 900 mOsm/L (left) and lower peak stress for ramping bath osmolarity from 300 to 100 mOsm/L (right)

The models presented in this paper showed a gradual improvement in the results and indicated the shortcoming of certain models. Combinations of different effective methods such as the normalization technique, DRS-CRS conversion, and the use of nonlinear elastic models and triphasic models will aid in better understanding the relaxation behavior of the UB. Improved parameter characterization will lead to better full organ models in the future.

BIBLOGRAPHY

BIBLIOGRAPHY

Abramowitch, Steven D., and Savio L-Y. Woo. "An improved method to analyze the stress relaxation of ligaments following a finite ramp time based on the quasi-linear viscoelastic theory." *J. Biomech. Eng.* 126.1 (2004): 92-97.

Baumgaertel, M., and H. H. Winter. "Determination of discrete relaxation and retardation time spectra from dynamic mechanical data." *Rheologica Acta* 28.6 (1989): 511-519.

Chantereau, P., et al. "Mechanical properties of pelvic soft tissue of young women and impact of aging." *International urogynecology journal* 25.11 (2014): 1547-1553.

Cost, Thomas L., and Eric B. Becker. "A multidata method of approximate Laplace transform inversion." *International journal for numerical methods in engineering* 2.2 (1970): 207-219.

Dahms, S. E., et al. "Composition and biomechanical properties of the bladder acellular matrix graft: comparative analysis in rat, pig and human." *British journal of urology* 82.3 (1998): 411-419.

Doehring, Todd C., Evelyn O. Carew, and Ivan Vesely. "The effect of strain rate on the viscoelastic response of aortic valve tissue: a direct-fit approach." *Annals of biomedical engineering* 32.2 (2004): 223-232.

Flack, Chandra, and C. R. Powell. "The worldwide economic impact of neurogenic bladder." *Current bladder dysfunction reports* 10.4 (2015): 350-354.

Fry, A. Wagg, CH. "Visco-elastic properties of isolated detrusor smooth muscle." *Scandinavian Journal of Urology and Nephrology* 33.201 (1999): 12-18.

Fung, Yuan-cheng. *Biomechanics: mechanical properties of living tissues*. Springer Science & Business Media, 1981.

Gupta, H. S., et al. "In situ multi-level analysis of viscoelastic deformation mechanisms in tendon collagen." *Journal of structural biology* 169.2 (2010): 183-191.

Goh, S. M., M. N. Charalambides, and J. G. Williams. "Determination of the constitutive constants of non-linear viscoelastic materials." *Mechanics of Time-Dependent Materials* 8.3 (2004): 255-268.

Kohandel, M., S. Sivaloganathan, and Giuseppe Tenti. "Estimation of the quasi-linear viscoelastic parameters using a genetic algorithm." *Mathematical and Computer Modelling* 47.3-4 (2008): 266-270.

Korossis, Sotirios, et al. "Regional biomechanical and histological characterisation of the passive porcine urinary bladder: Implications for augmentation and tissue engineering strategies." *Biomaterials* 30.2 (2009): 266-275.

Labus, Kevin M., and Christian M. Puttlitz. "Viscoelasticity of brain corpus callosum in biaxial tension." *Journal of the Mechanics and Physics of Solids* 96 (2016): 591-604.

Liu, Z., and K. Yeung. "The preconditioning and stress relaxation of skin tissue." *Journal of Biomedical & Pharmaceutical Engineering* 2.1 (2008): 22-28.

Maas, Steve, et al. "FEBio theory manual." *Musculoskeletal Research Laboratories, University of Utah, Salt Lake City, UT* (2011).

Martins, Pedro ALS, et al. "Uniaxial mechanical behavior of the human female bladder." *International urogynecology journal* 22.8 (2011): 991-995.

McDougall, Ian, Nese Orbey, and John M. Dealy. "Inferring meaningful relaxation spectra from experimental data." *Journal of Rheology* 58.3 (2014): 779-797.

Mun, Sungho, and Goangseup Zi. "Modeling the viscoelastic function of asphalt concrete using a spectrum method." *Mechanics of Time-Dependent Materials* 14.2 (2010): 191-202.

Nagatomi, Jiro, et al. "Changes in the biaxial viscoelastic response of the urinary bladder following spinal cord injury." *Annals of biomedical engineering* 32.10 (2004): 1409-1419.

Nagatomi, Jiro, et al. "Contribution of the extracellular matrix to the viscoelastic behavior of the urinary bladder wall." *Biomechanics and modeling in mechanobiology* 7.5 (2008): 395-404.

Natali, A. N., et al. "Bladder tissue biomechanical behavior: experimental tests and constitutive formulation." *Journal of biomechanics* 48.12 (2015): 3088-3096.

Park, S. W., and R. A. Schapery. "Methods of interconversion between linear viscoelastic material functions. Part I—A numerical method based on Prony series." *International journal of solids and structures* 36.11 (1999): 1653-1675.

Park, S. W., and Y. R. Kim. "Fitting Prony-series viscoelastic models with power-law presmoothing." *Journal of materials in civil engineering* 13.1 (2001): 26-32.

Polliack, T., et al. "Clinical and economic consequences of volume-or time-dependent intermittent catheterization in patients with spinal cord lesions and neuropathic bladder." *Spinal cord* 43.10 (2005): 615-619.

Roccabianca, Sara, and Tamara Reid Bush. "Understanding the mechanics of the bladder through experiments and theoretical models: Where we started and where we are heading." *Technology* 4.01 (2016): 30-41.

Roylance, David. "Engineering viscoelasticity." *Department of Materials Science and Engineering–Massachusetts Institute of Technology, Cambridge MA* 2139 (2001): 1-37.

Sarver, Joseph J., Paul S. Robinson, and Dawn M. Elliott. "Methods for quasi-linear viscoelastic modeling of soft tissue: application to incremental stress-relaxation experiments." *J. Biomech. Eng.* 125.5 (2003): 754-758.

Schapery, Richard Allan. "A simple collocation method for fitting viscoelastic models to experimental data." (1962).

Shanbhag, Sachin. "pyReSpect: A computer program to extract discrete and continuous spectra from stress relaxation experiments." *Macromolecular Theory and Simulations* 28.3 (2019): 1900005.

Shen, Zhilei Liu, et al. "Viscoelastic properties of isolated collagen fibrils." *Biophysical journal* 100.12 (2011): 3008-3015.

Tahmasbi, Rasool, and Sadegh Rezaei. "A two-parameter lifetime distribution with decreasing failure rate." *Computational Statistics & Data Analysis* 52.8 (2008): 3889-3901.

Thiruchelvam, Nikesh, et al. "Neurotransmission and viscoelasticity in the ovine fetal bladder after in utero bladder outflow obstruction." *American Journal of Physiology-Regulatory, Integrative and Comparative Physiology* 284.5 (2003): R1296-R1305.

Tschoegl, Nicholas W. *The phenomenological theory of linear viscoelastic behavior: an introduction*. Springer Science & Business Media, 1989.

Tuttle, T. and Roccabianca, S. "*Effects of swelling on urinary bladder wall mechanics*." 8th World Congress of Biomechanics, July 8-12, 2018, Convention Centre, Dublin, Ireland. Presentation.

Van Mastrigt, Ron, and J. C. Nagtegaal. "Dependence of the viscoelastic response of the urinary bladder wall on strain rate." *Medical and Biological Engineering and Computing* 19.3 (1981): 291-296.

Vincent, Julian. "Basic elasticity and viscoelasticity." *Structural biomaterials* 1 (2012): 1-28.

Zanetti, Elisabetta M., et al. "Bladder tissue passive response to monotonic and cyclic loading." *Biorheology* 49.1 (2012): 49-63.